

The average absorption properties of broad absorption line quasars at $800 < \lambda_{\text{rest}} < 3000 \text{ \AA}$, and the underlying physical parameters

Alexei Baskin,^{1*} Ari Laor¹ and Fred Hamann²

¹*Physics Department, Technion – Israel Institute of Technology, Haifa 32000, Israel*

²*Department of Astronomy, University of Florida, Gainesville, FL 32611-2055, USA*

ABSTRACT

Broad absorption line quasars (BALQs) present a large diversity in their broad absorption line (BAL) profiles. To investigate what physical parameters underlie this diversity, we construct a sample of BALQs which covers $\lambda_{\text{rest}} \approx 800 - 3000 \text{ \AA}$, based on the Sloan Digital Sky Survey DR7 quasar catalogue. The average BAL properties are evaluated by taking the ratios of average BALQ spectra to the average spectra of matched samples of non-BALQs, where the matching is based on various emission properties. We find the following properties. (i) There is no detectable Lyman edge associated with the BAL absorbing gas ($\tau < 0.1$). (ii) The known increase of average absorption depth with the ionization potential extends to the higher ionization N V and O VI BALs. We also find that the C IV BAL profile is controlled by two parameters. (i) The He II emission EW, which controls the typical velocity of the C IV BAL, but does not affect the absorption depth. (ii) The spectral slope in the 1700–3000 Å range (α_{UV1}), which controls the C IV peak absorption depth, but does not affect the typical velocity. The He II EW and α_{UV1} also control the observed fraction of quasars that are BALQs. We suggest that a lower He II EW may indicate a weaker ionizing continuum, which allows the outflow to reach higher velocities before being overionized, possibly without a need to invoke a shielding gas. A redder continuum may indicate a more inclined system, and a larger covering factor and larger column of the outflow along the line of sight.

Key words: galaxies: active – quasars: absorption lines – quasars: general.

1 INTRODUCTION

Broad absorption line quasars (BALQs) are a subtype of active galactic nuclei (AGN), defined by the presence of broad and blue-shifted absorption features (e.g., Weymann, Carswell & Smith 1981). The intrinsic fraction of BALQs from the total quasar population is estimated to be $\sim 15 - 20$ per cent (Hewett & Foltz 2003; Reichard et al. 2003; Knigge et al. 2008; Gibson et al. 2009. Allen et al. 2011 claim it can be as high as ~ 40 per cent). While there are several differences in emission properties between BALQs and non-BALQs, BALQs appear to be drawn from the non-BALQ population (Weymann et al. 1991; Hamann, Korista & Morris 1993; Reichard et al. 2003). Broad absorption lines (BALs), and the C IV BAL in particular, span a large range in depth, width and overall velocity shift (v_{shift}) between different objects. For most BALQs, absorption is observed only in

high-ionization lines (these objects are termed ‘HiBALQs’). For a smaller fraction of BALQs, absorption is also observed in low-ionization lines, e.g. Mg II (‘LoBALQs’). The predominant unifying model states that the difference between the AGN subtypes is our viewing angle towards the quasar central regions (e.g., Elvis 2000). However, an alternative scenario suggests that LoBALQs are an evolutionary stage of AGN, in which the nucleus expels a surrounding dusty ‘cocoon’ (Voit, Weymann & Korista 1993; Urrutia et al. 2009; Farrah et al. 2010, 2012; Glikman et al. 2012; cf. Lazarova et al. 2012).

What are the average BALQ spectral properties shortward of Ly α , and near the Lyman limit? Most of BALQ studies analyse spectra only down to λ_{rest} of Si IV (e.g., Gibson et al. 2009; Allen et al. 2011) or N V (e.g., Weymann et al. 1991). In this study, we utilize the Sloan Digital Sky Survey (SDSS; York et al. 2000) DR7 quasar catalogue (Schneider et al. 2010; Shen et al. 2011), and investigate high- z (> 3) object spectra, which cover λ_{rest} from C IV down to $\sim 800 \text{ \AA}$. The spectra of $z > 3$ quasars

* E-mail: alexei@physics.technion.ac.il

are heavily absorbed by the intervening Lyman forest at $\lambda_{\text{rest}} < 1216 \text{ \AA}$. We overcome this foreground absorption and derive the BALQ intrinsic absorption by taking the ratio of the average spectrum of BALQs and the average spectrum of a matched control sample of non-BALQs. The ratio spectrum allows us to place a limit on the average Lyman edge depth associated with the BAL systems, and thus a limit on the covering factor (CF) of low ionization BAL system. We also extend earlier studies on the average absorption strength of C II, Si IV and C IV to the higher ionization N V and O VI BALs.

The ratio spectrum is meaningful only if the average emission properties of BALQs and non-BALQs are indeed the same. Various studies find systematic differences between the intrinsic emission properties of BALQs and non-BALQs. There are reports that BALQs are located on the high- L and high- L/L_{Edd} end of the Boroson & Green (1992) eigenvector 1 (Boroson 2002). BALQs are observed to have larger blueshifts of C IV emission than non-BALQs (Richards et al. 2002; Reichard et al. 2003), and LoBALQs to have the highest blueshifts (Richards et al. 2002). BALQs are found to be redder than non-BALQs (Reichard et al. 2003; Maddox et al. 2008; Gibson et al. 2009; Allen et al. 2011), and LoBALQs to be redder than HiBALQs (Weymann et al. 1991; Sprayberry & Foltz 1992; Boroson & Meyers 1992; Reichard et al. 2003; Gibson et al. 2009). The reddening is interpreted by some authors as a result of BALQs being viewed preferentially closer to edge on (e.g., Ogle et al. 1999), or as an imprint of a dusty ‘cocoon’ (see references above). Trump et al. (2006) find the emission lines to be broader for BALQs than for non-BALQs. BALQs are reported to have lower C IV equivalent width (EW) than non-BALQs, X-ray weaker BALQs are observed to have stronger BALs with larger terminal velocities, and the measured velocities are larger for higher- L_{UV} BALQs (Brandt, Laor & Wills 2000; Laor & Brandt 2002; Gibson et al. 2009). LoBALQs show the strongest and broadest high-ionization absorption lines (Allen et al. 2011).

Thus, to make a more accurate ratio spectrum one needs to use samples of BALQs and non-BALQs with a similar distribution of intrinsic emission properties. One can then take another step, and explore whether the derived absorption properties, in particular the average C IV absorption profile, depend on the intrinsic emission properties, such as L/L_{Edd} . For this purpose, we expand our study to $z \sim 1.5$ quasars, where one can observe the 1400–3000 Å range, and derive emission parameters, such as L/L_{Edd} , based on the Mg II $\lambda 2798$ broad emission line. Despite numerous studies, the intrinsic properties which underlie the diversity of BALs remain elusive. This study allows us to address what causes the large diversity of the observed BAL properties

We explore in this study the dependence of the C IV BAL properties on the He II EW and on the UV slope (α_{UV}). This exploration is motivated by the following. The He II EW is a measure of the strength of the extreme UV (EUV) continuum above 54 eV, compared to the near UV continuum, and there are reports that BALQs have on average lower He II EW than non-BALQs (Richards et al. 2002; Reichard et al. 2003). A Broad Line Region (BLR) wind component is reported to be affected by the ionizing continuum hardness (Leighly & Moore 2004, based on He II EW; Kruczek et al. 2011, based on α_{ox}), and the BLR

wind component is suggested by Richards (2012) to be possibly relevant to the BALQ phenomenon. In addition, α_{UV} is correlated with reddening (e.g., Baskin & Laor 2005; Stern & Laor 2012), and since reddening is more common in BALQs (see above), this implies a possible relationship between α_{UV} and BALQ properties.

The paper is structured as follows. The data analysis method is described in Section 2. In Section 3 we analyse composite spectra of the BALQ and non-BALQ samples, find a trend between the ionization potential and the average BAL depth, and constrain the average H⁰ absorber properties. In Section 4 we investigate what parameters span the C IV BAL properties. A physical interpretation to our findings is proposed in Section 5. In Section 6 we examine which dust extinction laws can explain the BALQ reddening relative to non-BALQs. Our conclusions are summarized in Section 7.

2 THE DATA ANALYSIS

The data set is drawn from the SDSS DR7. The object BALQ classification is adopted from the Shen et al. (2011) quasar catalogue.¹ Shen et al. (2011) use the Gibson et al. (2009) BALQ classification for objects that are included in the SDSS DR5, and classify the remaining objects based on a visual inspection of the C IV region. Note that Gibson et al. (2009) use a modified version of ‘balnicity index’ (BI) of Weymann et al. (1991) to detect BALQs, which they term BI₀. They integrate the continuum-normalized spectral flux starting from a blueshift of 0, rather than -3000 km s^{-1} used in the traditional BI. We include in the data set only objects with $S/N \geq 3$ in the SDSS i -filter, to avoid unusually low- S/N spectra (the S/N criterion excludes $\sim 5 - 10$ per cent of the objects; see below). We divide the data set into two subsets that cover different λ_{rest} ranges as described below.

(i) The $800 \leq \lambda_{\text{rest}} \leq 1750 \text{ \AA}$ range i.e., $3.75 \leq z \leq 4.25$ for the SDSS (hereafter, the ‘high- z ’ sample). The lower limit on z is set to allow a detection of Lyman limit absorption intrinsic to the BALQs, and the upper limit is set to detect the continuum redward of the C IV emission complex. The DR7 covers this z range for 228 BALQs and 1320 non-BALQs. The $S/N \geq 3$ criterion leads to 200 BALQs and 1142 non-BALQs.

(ii) The $1400 \leq \lambda_{\text{rest}} \leq 3000 \text{ \AA}$ range i.e., $1.75 \leq z \leq 2.05$ for the SDSS (hereafter, the ‘low- z ’ sample). The lower and upper limits are placed to cover the C IV BAL and the Mg II emission line, respectively. The DR7 contains 1691 BALQs and 13,388 non-BALQs in this range. The S/N criterion excludes 39 BALQs and 739 non-BALQs. Since LoBALQs are a distinct subtype of BALQs, with redder spectra than the more common HiBALQs (Weymann et al. 1991; Sprayberry & Foltz 1992; Boroson & Meyers 1992; Reichard et al. 2003; Gibson et al. 2009), we exclude from the low- z BALQ sample 56 objects with a detected Mg II

¹ The updated Shen et al. (2011) quasar catalogue, available at <http://das.sdss.org/va/qso-properties-dr7/dr7.htm>, includes the improved z from Hewett & Wild (2010).

BAL (Shen et al. 2011), and construct a sample of low- z HiBALQs only. We do not construct a similar high- z HiBALQ sample, as it is not clear which low-ionization absorption line at $\lambda_{\text{rest}} \leq 1750 \text{ \AA}$ matches the Mg II absorption line. Note that Shen et al. (2011) do not conduct a systematic search for Mg II BALQs in the post-DR5 quasar sample, and report only serendipitously found Mg II BALQs for this sample. Thus, the exclusion of LoBALQs from the low- z BALQ sample might be incomplete. Trump et al. (2006) report a Mg II BALQ fraction of 1.3 per cent of quasars for DR3 (i.e. 164 objects in our sample), where BALs are detected using the ‘absorption index’ $\text{AI} > 0$ criterion, while Allen et al. (2011), who use the $\text{BI} > 0$ criterion, find a smaller fraction of 0.3 per cent for DR6 (38 objects). The different fractions result from the different definitions of AI and BI.² Thus, our low- z HiBALQ sample is likely contaminated by ~ 100 LoBALQs which pass the $\text{AI} > 0$ criterion, but none of these pass the $\text{BI} > 0$ criterion. The final low- z sample is comprised of 1596 HiBALQs and 12,649 non-BALQs.

Since the spectra of high- z objects have a relatively low S/N (a median value of ~ 7 per resolution element at continuum regions unaffected by absorption and strong emission)³, the spectra are smoothed by a 22 pixel-wide moving average filter, which allows to achieve a median S/N of ~ 22 per resolution element [the filter width is equivalent to ~ 9 resolution elements i.e., $\sim 1350 \text{ km s}^{-1}$ (York et al. 2000)]. The spectra of low- z objects are smoothed by the same filter, yielding a median S/N of ~ 66 per resolution element. Since we are dealing with BALs (i.e., line width $> 2000 \text{ km s}^{-1}$), the absorption profiles explored in this study remain well resolved. All spectra are normalized by the mean flux density in the $\lambda_{\text{rest}} = 1700 - 1720 \text{ \AA}$ range.⁴

Median spectra are calculated by utilizing a modified median method. A simple mean is not adopted as the representative average spectrum, since it can be affected by outliers. Outliers have a negligible effect on the median, but the median yields a relatively ‘noisier’ composite compared to the mean. We utilize a modified median method, which is a hybrid between the standard median and the mean, and which mitigates the shortcomings of the two methods. First, the object spectra are sorted based on the normalized $f_{\lambda}(\lambda_{\text{rest}})$. Then, 10 per cent of the objects above and 10 per cent of the objects below the median are marked. Finally, the mean f_{λ} of the marked objects is adopted as the composite f_{λ} at a given λ_{rest} (a similar method is used to calculate the Libor interest rate in Economy).

The intrinsic BALQ absorption is evaluated by utilizing the non-BALQ sample. The non-BALQ composite is assumed to represent the intrinsically unabsorbed emission of the BALQs (the construction of composites matched in

emission properties is described below). The ratio between the BALQ and non-BALQ composites (hereafter the R spectrum) is interpreted as the intrinsic BALQ absorption spectrum. Since the ratio does not remove an overall spectral energy distribution (SED) differences between BALQs and non-BALQs, we fit a straight-line continuum across the profile from $v_{\text{shift}} = 0$ to $-30,000 \text{ km s}^{-1}$. A residual Si IV emission, if present, has little effect on the C IV measurements. The caveat of our approach is that if there are significant intrinsic differences in line emission within the absorbed region for BALQs, then the derived absorption profile will be biased.

The individual absorption profiles are often characterized by a relatively narrow absorption peak. This characteristic profile is smeared out when forming the composite, due to the distribution of peak absorption velocities. In order to investigate the median ‘BAL rest-frame’ absorption profile near the absorption peak, we also form a composite based on the aligned C IV peak-absorption. This composite, calculated for the high- z BALQs, allows to detect relatively narrow ($\text{FWHM} \gtrsim 1500 \text{ km s}^{-1}$) and weak absorption lines which are otherwise heavily blended in the crowded FUV region, and also provides some hint on the optical depth of resolved multiplet absorption. The BALQ spectra are aligned by shifting each spectrum in velocity, so that the maximum absorption of C IV falls at the same velocity for all spectra. Then, a composite of the aligned spectra is calculated. The 22-pixel spectral smoothing by a relatively broad filter, smooths out any narrow features ($\lesssim 500 \text{ km s}^{-1}$) superimposed on the C IV BAL, and reduces their effect on the alignment procedure. When the matched non-BALQ sample is constructed, a similar distribution of velocity shifts is used.

We study the dependence of the BALQ absorption properties on the following parameters.

(i) The He II EW, which may serve as a measure of the EUV ionizing SED hardness. The He II EW is measured by integrating the normalized f_{λ} in the $\lambda_{\text{rest}} = 1620 - 1650 \text{ \AA}$ range, assuming $f_{\lambda}^{\text{cont}} = 1$ i.e., a constant $f_{\lambda}^{\text{cont}}$ between the normalization window (1700–1720 \AA) and $\sim 1620 \text{ \AA}$. The adopted λ_{rest} range minimizes contributions from C IV and O III] $\lambda\lambda 1661, 1666$ to the evaluated He II EW. Using a constant $f_{\lambda}^{\text{cont}}$ corresponds to a spectral slope of $\alpha = -2$ ($f_{\nu} \propto \nu^{\alpha}$), which serves as a rough approximation for the local slope (Section 4.2). A significantly more accurate derivation of the local $f_{\lambda}^{\text{cont}}$ is hindered by the C IV BAL for BALQs. The derived He II EW is slightly overestimated in objects where the continuum slope is bluer, but these objects tend to have a higher He II EW, where the exact continuum placement is less significant. The constant $f_{\lambda}^{\text{cont}}$ is a good approximation in the low He II EW objects. In the reddest objects, the continuum at $\lambda_{\text{rest}} < 1700 \text{ \AA}$ drops below the adopted constant $f_{\lambda}^{\text{cont}}$, leading to slightly negative He II EW (see Section 4.3). The small errors in the absolute values of the He II EW are significantly smaller than the trends with the He II EW explored below.

(ii) The UV spectral slope α_{UV} , which may serve as a measure of dust absorption. For the high- z sample, the slope is evaluated between the 1275–1285 and 1700–1720 \AA windows, and is denoted as α_{UVs} . The latter window is redward of O III] $\lambda 1665$ emission and the C IV emission ‘shelf’, and

² $\text{AI} > 0$ ($\text{BI} > 0$) requires at least one continuous absorption trough with a minimal absorption depth of 0.1 and a minimal width of 1000 km s^{-1} (2000 km s^{-1}) in the $-29,000 < v_{\text{shift}} < 0 \text{ km s}^{-1}$ ($-25,000 < v_{\text{shift}} < -3000 \text{ km s}^{-1}$) range.

³ The S/N of an object is estimated by calculating the ratio between the mean and standard deviation of f_{λ} in the $\lambda_{\text{rest}} = 1700 - 1720 \text{ \AA}$ window.

⁴ It should be noted that the wavelength used for the normalization is not significant, as verified by repeating the main analysis using the $\lambda_{\text{rest}} = 1275 - 1285 \text{ \AA}$ range instead.

blueward of N III] $\lambda 1750$. The former window is between the red wing of Ly α +N v emission complex and O I $\lambda 1303$. The window between O I $\lambda 1303$ and C II $\lambda 1335$ is not utilized, because it is affected by C II and Si IV absorption in BALQs. For the low- z sample, the slope is evaluated between the 1700–1720 and 2990–3010 Å windows, and is denoted as α_{UV1} . The latter window is redward of Mg II $\lambda 2798$.

We also explore the dependence of the BALQ absorption, for the low- z sample, on the following additional parameters.

- (i) $L(3000\text{\AA})$, taken from Shen et al. (2011).
- (ii) Mg II FWHM, taken from Shen et al. (2011).
- (iii) M_{BH} , estimated using parameters (i) and (ii), and the Vestergaard & Osmer (2009) prescription (values listed in Shen et al. 2011).
- (iv) L/L_{Edd} , evaluated as $\log L/L_{\text{Edd}} = \log L(3000\text{\AA}) - \log M_{\text{BH}} - 37.4$, where we adopt a bolometric correction factor of 5.15 (Shen et al. 2008).

We do not use the C IV emission line to estimate M_{BH} given the significant uncertainties associated with this line (e.g. Baskin & Laor 2005, and citations thereafter). The objects are binned for each parameter, so that each BALQ bin contains the same number of objects. The corresponding non-BALQ bins span the same parameter range, but the distribution of objects within each bin may be different. A median composite spectrum is calculated for each bin.

3 THE AVERAGE BALQ PROPERTIES

Figure 1 presents a comparison between the high- z BALQ and non-BALQ composites, aligned by their tabulated z . We present both the median and the mean composites, to demonstrate the level of systematics produced by the averaging procedure, which is larger than the purely statistical noise. The two composites are similar overall, except at wavelength regions of strong absorption and emission features (e.g., Ly α), where the mean composite is more affected by outliers. Bottom panel presents the R composite. The median and mean R composites are similar. There are small differences in absorption amplitude, which are likely selection effects.⁵ We indicate the laboratory wavelength location of absorption lines of various ionized species. There are many absorption lines in the $\lambda_{\text{rest}} = 800 - 900$ Å range, and the indicated absorption line locations are for illustration only. The steep decline of flux blueward of the Lyman edge for both BALQ and non-BALQ composites (top panel) is caused by intervening Lyman α systems. Observations of low- z AGN, which are unaffected by intervening Lyman systems, do not show this steep decline (Zheng et al. 1997; Telfer et al. 2002; Scott et al. 2004; Shull et al. 2012).

The three main features which can be seen in the R composites are: (i) there is no detectable Lyman limit absorption; (ii) the high ionization lines observed shortward of Ly α , in particular N v and O VI, show stronger absorption

than observed longward of Ly α ; (iii) the overall continuum ratio is red. These results are further discussed below.

Figure 2 compares the absorption profiles of Si IV, C IV, N v and O VI. The higher the ionization potential, the stronger is the BAL trough. The Si IV absorption line, produced by photons above 33.5 eV and destroyed by photons above 45.1 eV, has the shallowest trough. It is followed in trough depth and absorption EW by C IV, N v and O VI (47.9–64.5, 77.5–97.9 and 113.9–138.1 eV, respectively). The absorption EW (transmission at maximal absorption) is 5.8 (0.87), 9.3 (0.83), 24.6 (0.56) and 25.2 Å (0.46) for Si IV, C IV, N v and O VI, respectively. The N v absorption may be affected by Ly α at $v_{\text{shift}} = 0$. Note that C II $\lambda 1335$ falls on the same trend, as its absorption is weaker (EW $\lesssim 1$ Å) than Si IV (Fig. 1, bottom panel).

Our findings are consistent with the Allen et al. (2011) report that on average Si IV reaches smaller values of peak absorption than C IV. Gibson et al. (2009) and Allen et al. (2011) find that the C IV BI distribution has a marginally larger tendency towards higher values than Si IV. The difference in absorption depth likely implies difference in CF.

Figures 3 and 4 present the C IV peak-absorption aligned R spectrum and absorption line profiles, respectively. Line identifications are indicated in Fig. 3 at the line laboratory wavelength. The peak-absorption alignment method aligns all the BALs, including low-ionization BALs (e.g., C II $\lambda 1335$). The line profiles of the BALs are examined further in Fig. 4, where the lines are grouped vertically based on the ionization potential. The absorption profiles are dominated by the relatively narrow absorption component (FWHM ≈ 3000 km s⁻¹). Fig. 4 indicates that for several lines the absorption is saturated, as indicated by the similar absorption depth of doublet components with different oscillator strengths. The absorption profile in these cases is set by a velocity dependent CF (e.g., S VI $\lambda\lambda 933, 945$). Other lines are not saturated (e.g., Si IV $\lambda\lambda 1397, 1403$), as can be indicated by more quantitative analysis (e.g. Dunn et al. 2012, Capellupo et al. in prep. and Hamann et al. in prep.).

3.1 Constraints on the BAL H⁰ Column

Figure 4 can be utilized to constrain the average BAL H⁰ column $N(\text{H}^0)$, based on the Ly α absorption line. We begin by deriving $N(\text{H}^0)$ assuming a uniform foreground screen i.e., CF = 1. The Ly α absorption line resides within the N v absorption trough. We estimate the Ly α absorption depth by interpolating linearly between the two ‘shoulders’ at $v_{\text{shift}} = \pm 2000$ km s⁻¹ (Fig. 4), which yields a continuum $f_{\lambda} \approx 0.55$ at the line centre. The measured $f_{\lambda} \approx 0.42$ at the peak absorption implies a Ly α peak absorption of $\exp(-\tau_0) = 0.42/0.55 \approx 0.76$. Assuming a Maxwellian absorption profile with a velocity dispersion b parameter of 1000 km s⁻¹, yields $N(\text{H}^0) \simeq 1 \times 10^{15}$ cm⁻² (e.g., Draine 2011, eq. C.1). This $N(\text{H}^0)$ implies $\tau \simeq 0.01$ at the Lyman edge (e.g., Osterbrock 1989, eq. 2.4), which is consistent with a non-detection of the edge in the absorption-peak aligned R spectrum (Fig. 4, Ly lim. panel). However, the Ly α line and Lyman edge can be highly saturated, with $N(\text{H}^0)$ well above the derived value. In that case, the Ly α absorption profile reflects the CF of the saturated cold absorber, which is at least $1 - 0.76 = 0.24$. However, the observed Lyman edge region shows no detectable edge, i.e. $\tau \lesssim 0.1$, and im-

⁵ The reversal of the mean versus median R spectra at the C IV and O VI absorption troughs is not a significant result. It reflects the fact that the residual flux at the O VI trough is closer to zero than for C IV.

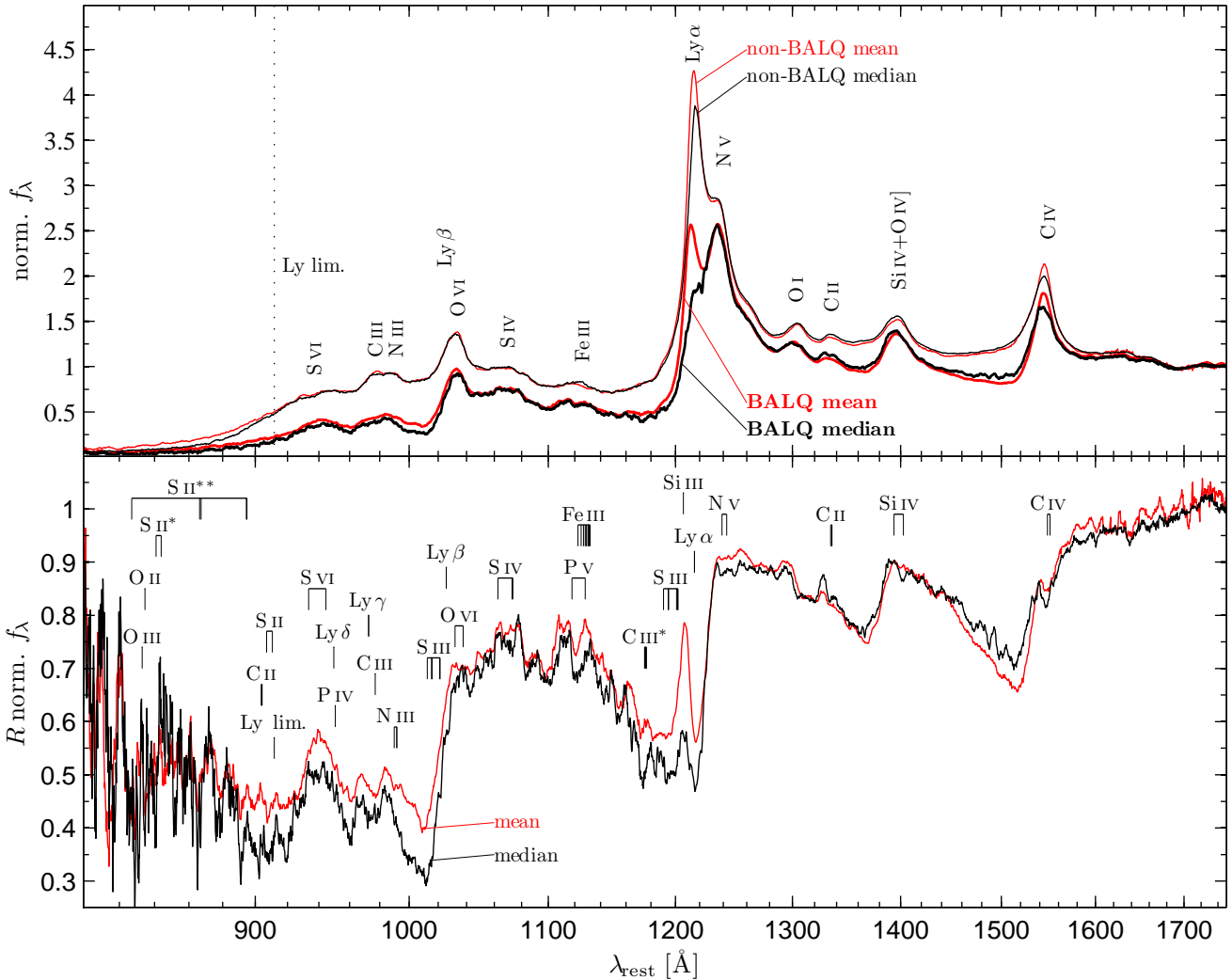


Figure 1. Comparison between the BALQ and non-BALQ composite spectra. Top panel: the median normalized flux of the BALQ and non-BALQ samples (thick and thin black solid line, respectively). The mean normalized flux is also presented for comparison (red lines). The composites can differ at strong absorption and emission features (e.g., Ly α), where the mean is more affected by outliers. The Lyman limit (vertical dotted line) and prominent emission lines are indicated. Bottom panel: the ratio between the BALQ and non-BALQ composites. The laboratory wavelength location of prominent absorption lines is indicated longward of the Lyman limit. We also indicate for reference the location of possible lines below the Lyman limit. The indicated S II* and S II** lines have excitation energy of 1.8 and 3.1 eV, respectively. There is no significant absorption edge detected at the Lyman limit. Note also the declining continuum ratio to the blue, and the increasing absorption features depths.

plies $N(\text{H}^0) < 1 \times 10^{17} \text{ cm}^{-2}$ if $\text{CF} = 0.24$. In addition, the Ly β shows only weak absorption, well below 0.24, if we adopt the O VI shoulder as the local continuum, which also suggests a non saturated Ly α absorption.

Another constraint on the CF of any nearly neutral saturated absorber can be derived from the C II $\lambda 1335$ absorption line. The R spectrum in the C II region shows $f_\lambda \approx 0.84$ at the line centre, compared to an estimated local continuum of 0.89 (Fig. 4, C II 1336 panel), which implies a $\text{CF} \lesssim 0.06$, consistent with the non detection of the expected Lyman edge absorption.

We note in passing that photoionization models indicate that the Ly α absorption should be at least as strong as Si IV for solar metallicity, regardless of the ionization parameter (Baskin & Laor 2012). This is consistent with our observations, as the Si IV absorption goes down from $f_\lambda \approx 0.9$ to

0.62 that indicates peak absorption of ~ 0.3 , which is similar to the Ly α peak absorption.

An obvious general caveat is that the above analysis is applied to the median absorption profile, and may not be valid to individual objects, such as LoBALQs, which are not excluded from the high- z BALQ sample.

4 WHICH PARAMETERS CONTROL THE ABSORPTION PROFILE?

In this section we use composite spectra to examine the relationship of C IV BAL properties to He II EW, α_{UV} , and other measured parameters.

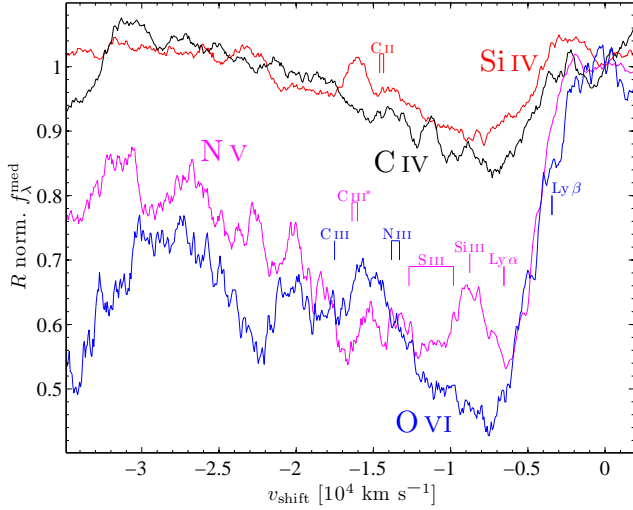


Figure 2. The absorption profiles of the prominent absorption lines Si IV, C IV, N V and O VI. The velocity scale is set by the longer wavelength of each doublet. The profiles are normalized to 1 at $v_{\text{shift}} = 0 \text{ km s}^{-1}$. Laboratory wavelength location of various other possible absorption lines is indicated by vertical tick marks (with the same colour coding). The absorption depth increases with the ionization potential of the absorbing ion.

4.1 C IV BAL trends with the He II EW

Figure 5 presents the high- z BALQ and non-BALQ samples separated into two bins based on their He II EW (as further described below). The upper panel presents the composite spectra of the two bins for BALQs and for non-BALQs, and the lower panel presents the R spectra for the two bins. The low He II EW bin displays a somewhat deeper and significantly broader C IV BAL, with peak absorption shifted to larger v_{shift} . This trend is also observed for Si IV and possibly for O VI, although a clear detection of the trend for the latter is hindered by the low S/N and the blending of a number of adjacent absorption lines. The trend does not appear significant for N V, probably due to contamination by the adjacent low ionization line Ly α , which is prominent relative to other low ionization lines (e.g., Fig. 3). The weaker trend between the He II EW and the N V and O VI BALs is further discussed in Section 5.1. The drop in the R spectrum at the red wing of the C IV emission line reflects a mismatch in the C IV emission EW between BALQs and non-BALQs for the same bin (see Fig. 5, top panel), and is most likely not an absorption effect. Table 1 summarizes various properties of the two He II EW bins, and lists the first three moments of the C IV absorption profile (EW, mean v_{shift} and dispersion σ).

Figure 6 presents the He II EW binning for the low- z sample, this time binned to 4 bins (as further described below), allowed by the larger sample size (see Section 2). The same trend of increasing depth and blueshift in the C IV absorption profile with decreasing He II EW is observed here as well. There is also an excess emission in the C III] + Si III] + Al III complex in the R spectra, which does not depend on the He II EW. The excess is related to a trend with α_{UV1} discussed below (Section 4.2). Table 2 lists the bin median properties, including the median Mg II FWHM, $L(3000\text{\AA})$, M_{BH} and L/L_{Edd} . It also presents the number of

LoBALQs with similar He II EW. LoBALQs are found predominantly in the lowest He II EW bin (43 out of 56 objects). In Appendix A we present a LoBALQ composite based on the 56 objects we excluded from our low- z sample in order to form the low- z HiBALQ sample (Section 2). The redder R spectrum of the lowest He II EW bin, compared to the other three, might represent a smooth transition between HiBALQs and LoBALQs, where the latter have the lowest He II EW and the reddest R spectrum (Appendix A). The smooth transition scenario can be further explored by analysing the Mg II BAL dependence on the He II EW and reddening in LoBALQs. This requires a larger sample of LoBALQs and is outside the scope of this paper.

Tables 1 and 2 list for each BALQ bin the observed BALQ fraction in DR7, which is defined as $f_{\text{BALQs}} \equiv N_{\text{BALQs}} / (N_{\text{BALQs}} + N_{\text{non-BALQs}})$. The tabulated errors on f_{BALQs} are minimal, and are based purely on number statistics. There is a strong trend between f_{BALQs} and the He II EW. For the low- z sample, f_{BALQs} goes up from 7.0 ± 0.4 per cent for the highest He II EW bin, to 23 ± 1 per cent for the lowest bin. For the high- z sample, a similar trend is found, and f_{BALQs} goes up from 11 ± 1 per cent for the high He II EW bin to 22 ± 2 per cent for the low He II EW bin.

4.2 C IV BAL trends with α_{UV}

Figures 7 and 8 explore the dependence of the BALQ absorption on α_{UV} . Figure 7 presents the high- z sample binned into two α_{UVs} bins. The C IV absorption profile follows the trend observed in the He II EW binning, where the redder α_{UVs} bin corresponds to the lower He II EW bin. Table 3 lists the bin median properties of the high- z sample. The median α_{UVs} of the BALQ bins is redder than the slope of the matched non-BALQ bins. Although the bins are matched by the α_{UVs} range (Section 2), the distribution of α_{UVs} values within the bin is different for the BALQs and non-BALQs. This slope difference yields the observed residual reddening of the R spectrum (Fig. 7, bottom panel). Figure 8 presents the low- z sample divided into four α_{UV1} bins. The trend with α_{UV1} is different from the trend with α_{UVs} . The low velocity C IV absorption profile becomes deeper as α_{UV1} becomes redder, while at higher velocities the C IV absorption profile remains unchanged. Table 4 summarizes the bin median properties. Note that the C III] + Si III] + Al III complex emission becomes stronger with redder α_{UV1} (Fig. 8, top panel), and the BALQ and non-BALQ matched composites have a similar complex emission.

The fraction of BALQs increases as the objects get redder. At the high- z sample, f_{BALQs} increases from 11 ± 1 to 26 ± 3 per cent, while at the low- z sample, f_{BALQs} increases from 6.9 ± 0.4 to 21 ± 1 per cent from the bluest to the reddest quartile. Most of the detected LoBALQs (44 out of 56) have slopes at least as red as the reddest bin, as expected (see Section 1).

4.3 C IV BAL trends with both He II EW and α_{UV}

Figure 9 shows a zoom-in on the C IV absorption profile for the low- z sample, and highlights the strong and different trends between the C IV BAL properties and the He II EW and α_{UV1} (not true for α_{UVs}). The He II EW

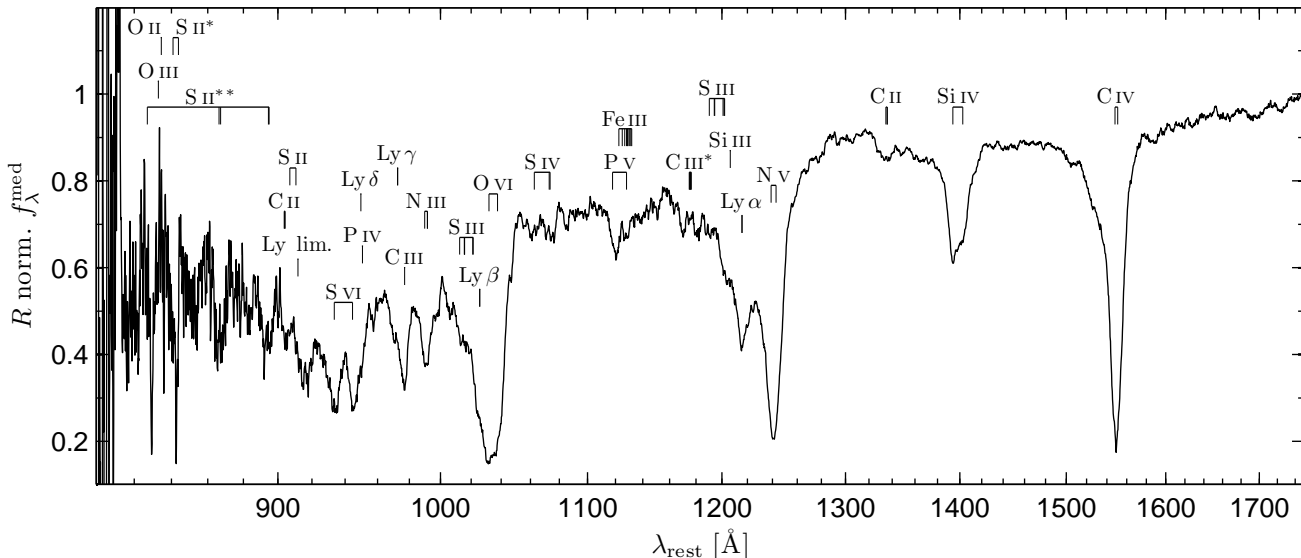


Figure 3. The absorption profiles near the absorption peak. The spectra are aligned so that the C IV absorption dip falls at 1549.48 Å (i.e., a 1:1 contribution to absorption from the two components of C IV $\lambda\lambda$ 1548.20, 1550.77). Note that both the low- and the high-ionization BALs are at the same v_{shift} as C IV. This allows to separate heavily blended features, such as Ly α and N V, and to detect weak and relatively narrow features, which are otherwise heavily blended, such as S VI (Fig. 1).

Table 1. The median properties of the He II EW binned high- z objects.

Class	Bin	N_{obj}	He II EW [Å]	α_{UVs}^a	EW [Å]	C IV BAL ^b		f_{BALQs}^c [per cent]
						$v_{\text{shift}}^{\text{mean}}$ [km s ⁻¹]	σ [km s ⁻¹]	
BALQs	high	100	5.4	-1.04	12.0	-13000	6800	11 ± 1
	low	100	0.4	-1.76	14.8	-12500	4700	22 ± 2
non- BALQs	high	778	6.1	-0.71				
	low	353	0.7	-1.36				

^a Measured between 1280 and 1710 Å ($f_{\nu} \propto \nu^{\alpha}$).

^b Measured between $v_{\text{shift}} = 0$ and $-30,000$ km s⁻¹.

^c Measured from the total quasar population. Errors are based on number statistics.

Table 2. The median properties of He II EW binned low- z objects.

Class	N_{bin}	N_{obj}	He II EW [Å]	α_{UVI}^a	log $L(3000\text{Å})$ [erg s ⁻¹]	Mg II FWHM [km s ⁻¹]	log M_{BH} [M_{\odot}]	log L/L_{Edd}	N_{LoBALs}^b	EW [Å]	C IV BAL ^c		f_{BALQs}^d [per cent]
											$v_{\text{shift}}^{\text{mean}}$ [km s ⁻¹]	σ [km s ⁻¹]	
BALQs	1	399	7.0	-0.97	45.90	3900	9.03	-0.48	7	7.8	-4600	2500	7.0 ± 0.4
	2	399	4.7	-0.83	45.97	4400	9.14	-0.52	1	13.9	-9200	5700	10.3 ± 0.5
	3	399	3.0	-0.79	46.00	4100	9.09	-0.44	5	15.7	-10900	5900	14.1 ± 0.8
	4	399	0.9	-0.96	45.99	3400	8.93	-0.30	43	22.5	-11900	6000	23 ± 1
non- BALQs	1	5330	7.3	-0.77	45.81	3800	8.93	-0.49					
	2	3461	4.7	-0.65	45.93	4000	9.03	-0.47					
	3	2425	3.1	-0.61	45.94	3700	8.98	-0.38					
	4	1368	1.0	-0.69	45.93	3300	8.87	-0.30					

^a Measured between 1710 and 3000 Å ($f_{\nu} \propto \nu^{\alpha}$).

^b Number of LoBALQs (identified based on a detection of Mg II BAL; Shen et al. 2011) with He II EW within or nearest to the bin range.

^c Measured between $v_{\text{shift}} = 0$ and $-30,000$ km s⁻¹.

^d Measured from the total quasar population. Errors are based on number statistics.

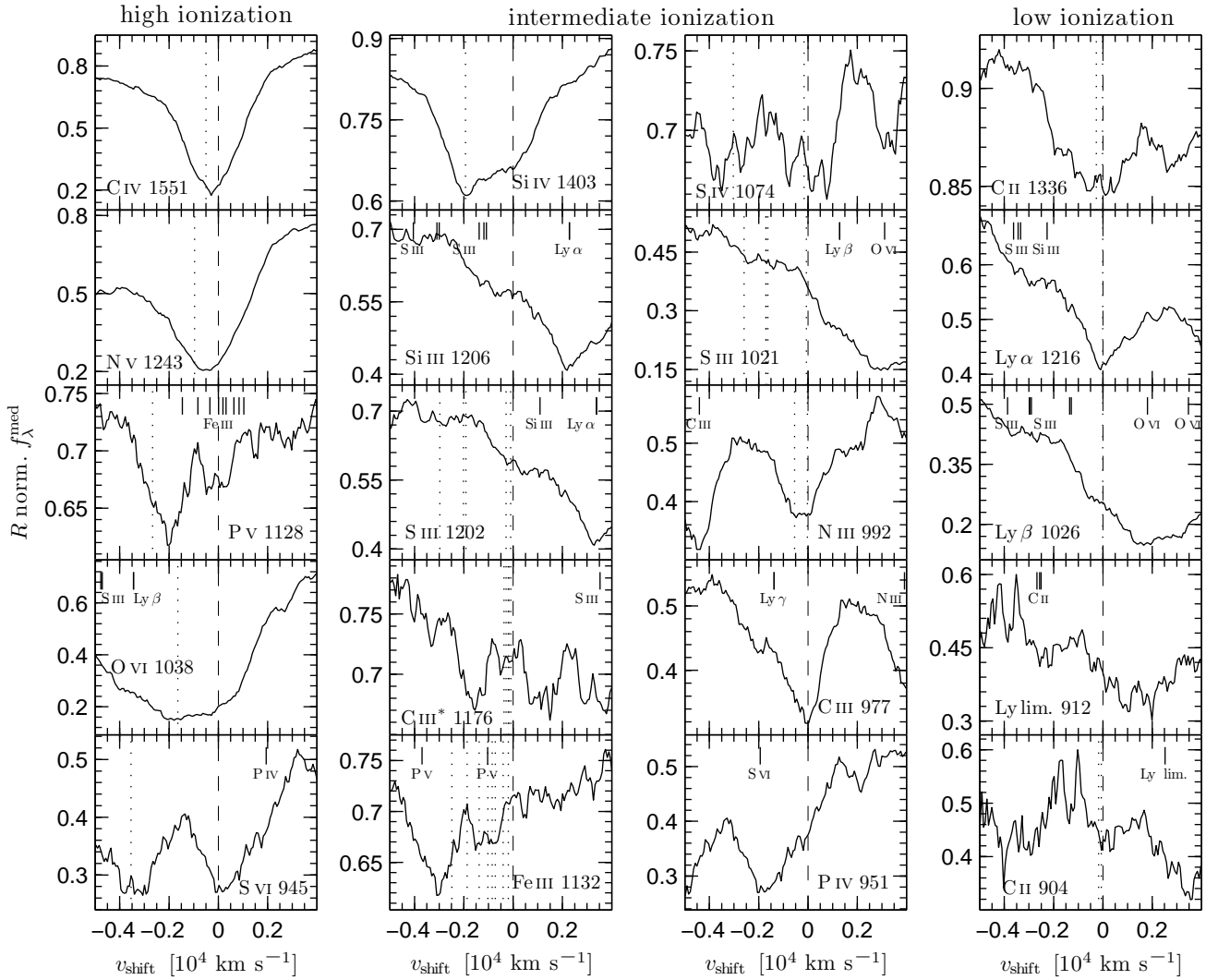


Figure 4. Line profiles of the aligned composite spectrum (see Fig. 3). The lines are grouped according to the ionization potential, and are arranged from the longer to the shorter wavelength at each group. The velocity scale is calculated relative to the redder line of each multiplet, which is indicated at each panel. A zero velocity shift and v_{shift} of other absorption lines of each multiplet are marked (dashed and dotted line, respectively). The location of other absorption lines is indicated by vertical tick marks at the top of each panel. Note that some of the doublets appear optically thick (e.g., S VI 945), while others appear unsaturated (e.g., Si IV 1403).

Table 3. The median properties of α_{UVs} binned high- z objects.^a

Class	Bin	N_{obj}	α_{UVs}	He II		C IV BAL ^b		f_{BALQs}^c
				EW [Å]	EW [Å]	$v_{\text{shift}}^{\text{mean}}$ [km s ⁻¹]	σ [km s ⁻¹]	
BALQs	blue	100	-0.92	4.8	7.9	-11700	6300	11 ± 1
	red	100	-1.90	1.2	17.2	-12600	4800	26 ± 3
non-BALQs	blue	848	-0.72	5.3				
	red	282	-1.66	1.2				

^a Measured between 1280 and 1710 Å ($f_{\nu} \propto \nu^{\alpha}$).

^b Measured between $v_{\text{shift}} = 0$ and $-30,000$ km s⁻¹.

^c Measured from the total quasar population. Errors are based on number statistics.

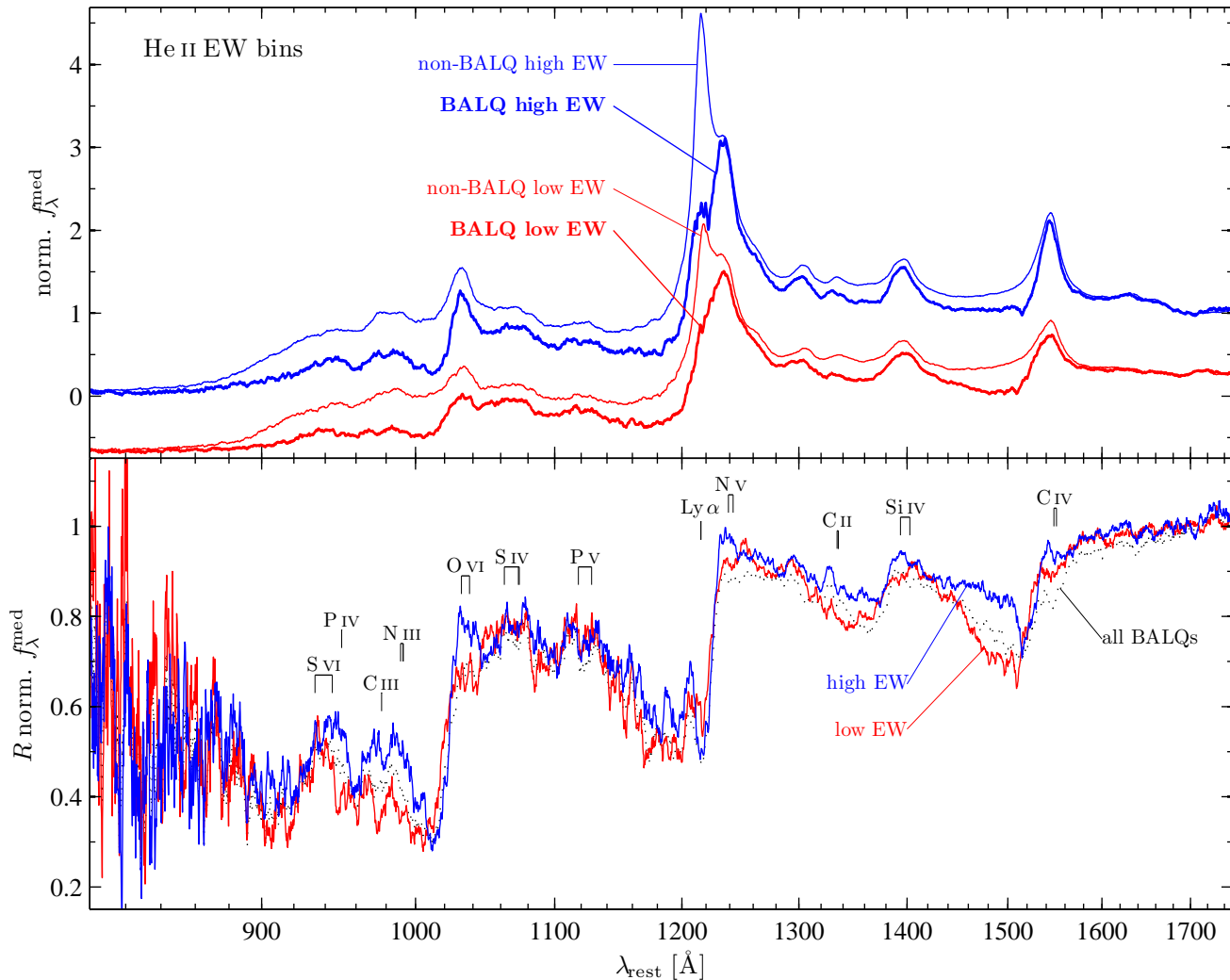


Figure 5. The dependence of the intrinsic absorption on the He II EW for the high- z sample. Top panel: the composite spectra of high and low He II EW BALQs and non-BALQs. The low He II EW spectra are shifted down by 0.7 for presentation purposes. Bottom panel: the ratio between the corresponding BALQ and non-BALQ bins. The ratio of the complete samples is also presented (same as in Fig. 1), which shows an apparent red side absorption in C IV that results from the different median C IV emission profiles in BALQs and non-BALQs. This effect is partly compensated by using the two subsamples, which have better matched C IV emission strengths. Note the significantly stronger C IV absorption for the lower He II EW composite. A similar effect is seen in the S IV BAL, some effect may be seen in the O VI BAL, and only a marginal effect is seen in N V, possibly due to blending with the low ionization Ly α BAL.

mostly controls the characteristic absorption v_{shift} , while α_{UV1} mostly controls the absorption depth, in particular at $v_{\text{shift}} < 10,000 \text{ km s}^{-1}$. Thus, it appears that the He II EW and α_{UV1} are independent parameters which span the C IV absorption profile properties. Their independence can also be inferred from Table 2, which shows similar median α_{UV1} values in the different He II EW bins, and similarly in Table 4, where the different α_{UV1} bins show similar median He II EW values. This is in contrast with the high- z sample, where α_{UVs} and the He II EW are correlated (Tables 1 and 3).

The highest He II EW and the bluest α_{UV1} bins may be incomplete in other BALQ studies based on a BI selection. A value of $\text{BI} > 0$ requires a BAL with a significant absorption (> 10 per cent) at least down to $v_{\text{shift}} = -5000 \text{ km s}^{-1}$ (given a minimal width of 2000 km s^{-1} , starting at $v_{\text{shift}} = -3000 \text{ km s}^{-1}$, Weymann et al. 1991). Since we find that

v_{shift} decreases with increasing He II EW, the highest He II EW bin might be missing yet lower v_{shift} BALQs, with peak absorption at $v_{\text{shift}} > -3000 \text{ km s}^{-1}$. Similarly, BALQs residing in the bluest α_{UV1} bin may be missed, since the peak-absorption is $\lesssim 10$ per cent for this bin (Fig. 9). Our sample is derived based on a BI_0 and visual selection (see Section 2), where $\text{BI}_0 > 0$ requires significant absorption (> 10 per cent) at least down to $v_{\text{shift}} = -2000 \text{ km s}^{-1}$. Thus, large He II EW, low v_{shift} BALQs are probably not missing in our sample, but weak BALs ($\lesssim 5$ per cent) possibly present in BALQs with the bluest α_{UV1} may be missing.

Figure 10 explores the C IV BAL dependence on the He II EW for different values of α_{UV1} . We divide the low- z sample into 4×4 bins based on α_{UV1} and the He II EW. First, the BALQ sample is divided into four α_{UV1} ‘parent’ bins, and matched non-BALQ bins are constructed (same procedure as in Fig. 8). Then, each α_{UV1} parent bin is divided

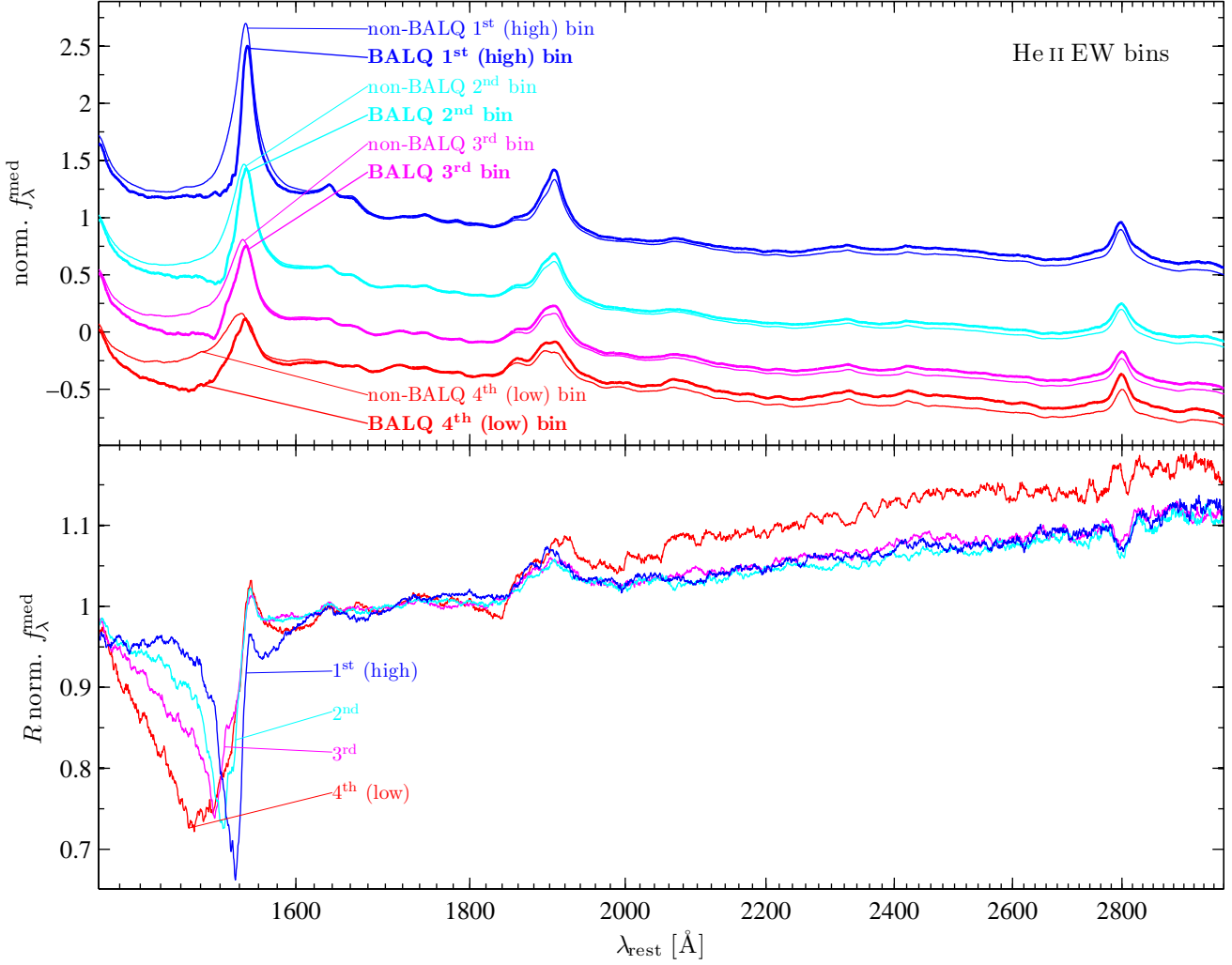


Figure 6. Same as Fig. 5, for the low- z sample. The BALQ and non-BALQ samples are divided here to four subsamples. The 2nd to 4th bin spectra in the upper panel are shifted down for presentation purposes by 0.6, 1 and 1.3, respectively. The C IV absorption profile becomes stronger and broader with lower He II EW values, as seen in the high- z sample (Figure 5).

Table 4. The median properties of α_{UV1} binned low- z objects.^a

Class	N_{bin}	N_{obj}	α_{UV1}	He II EW [Å]	\log $L(3000\text{Å})$ [erg s ⁻¹]	Mg II FWHM [km s ⁻¹]	\log M_{BH} [M_{\odot}]	\log L/L_{Edd}	N_{LoBALs}^b	C IV BAL ^c EW [Å]	$v_{\text{shift}}^{\text{mean}}$ [km s ⁻¹]	σ [km s ⁻¹]	f_{BALQs}^d [per cent]
BALQs	1	399	-0.48	3.5	45.92	4100	9.08	-0.49	3	7.6	-10900	6200	6.9 ± 0.4
	2	399	-0.76	4.0	45.97	4100	9.09	-0.45	3	8.2	-9000	5600	10.7 ± 0.6
	3	399	-1.05	4.3	45.97	3900	9.05	-0.41	6	6.8	-4700	2300	14.5 ± 0.8
	4	399	-1.51	3.5	46.00	3600	9.02	-0.38	44	10.3	-4500	2500	21 ± 1
non- BALQs	1	5414	-0.44	4.6	45.86	3800	8.96	-0.46					
	2	3334	-0.76	5.4	45.92	3800	8.99	-0.43					
	3	2349	-1.02	5.9	45.89	3700	8.97	-0.42					
	4	1526	-1.45	5.1	45.86	3600	8.92	-0.41					

^a Measured between 1710 and 3000 Å ($f_{\nu} \propto \nu^{\alpha}$).

^b Number of LoBALQs (identified based on a detection of Mg II BAL; Shen et al. 2011) with α_{UV1} within or nearest to the bin range.

^c Measured between $v_{\text{shift}} = 0$ and $-30,000$ km s⁻¹.

^d Measured from the total quasar population. Errors are based on number statistics.

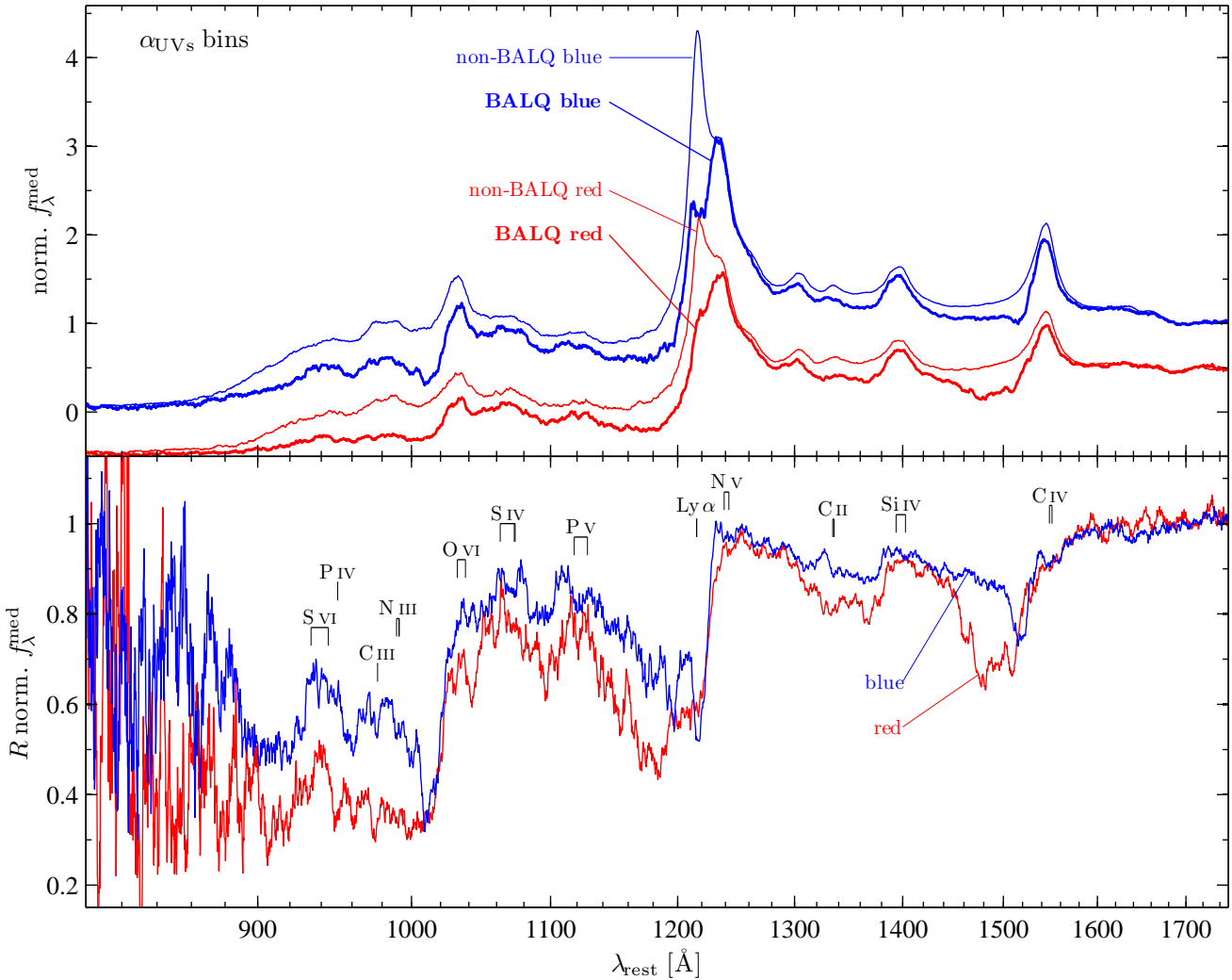


Figure 7. The dependence of the intrinsic absorption on the α_{UVs} for the high- z sample. Top panel: the composite spectrum of BALQ and non-BALQ subsamples matched in α_{UVs} range. The BALQ and non-BALQ red bins are shifted down by 0.5 for presentation purposes. Bottom panel: the ratio between the corresponding BALQ and non-BALQ composites. Note the stronger absorption for the redder α_{UVs} . There is a residual reddening of the R spectrum, since the median slope of the BALQ bin is redder than the slope of matched non-BALQ bin.

into four He II EW bins, with matching non-BALQs from the corresponding α_{UV1} non-BALQ bin. As Fig. 10 shows, the C IV absorption at a given α_{UV1} , shifts to higher v_{shift} as the He II EW decreases, at all four α_{UV1} bins. Also, the maximum absorption depth at all He II EW bins, gets larger as α_{UV1} gets redder. The change in v_{shift} is most prominent for the bluest two bins. Table 5 lists the median properties for the 4×4 bins. Note that the reddest and lowest He II EW BALQ and non-BALQ bins have median He II EW < 0 . This is an artefact which results from measuring the EW by using the continuum at 1700–1720 Å, where in the reddest and weakest He II objects the flux density at He II is lower than at 1700–1720 Å, leading to a negative EW (Section 2). The negative He II EW has no effect on the binnings, which are independent of the absolute He II EW values. The value of f_{BALQs} increases with decreasing He II EW, at a given α_{UV1} , and also as α_{UV1} gets redder, at a given He II EW. We find the smallest value of $f_{\text{BALQs}} = 4.2 \pm 0.4$ per cent in the highest He II EW and bluest α_{UV1} bin, increasing to 31 ± 4

per cent in the lowest He II EW and reddest α_{UV1} bin. Most of the LoBALQs (33/56) reside in the reddest and lowest He II EW bin.

4.4 C IV BAL dependence on other emission properties

Figure 11 investigates whether a certain physical property underlies the above relations between the absorption profile and the He II EW and α_{UV1} . The figure presents the C IV BAL profile for samples binned based on the Mg II FWHM, $L(3000\text{Å})$, M_{BH} and L/L_{Edd} values. Table 6 lists the property median value of each bin for each of the 4 binning procedures. There is no trend in the absorption profile with $L(3000\text{Å})$. There is a trend of stronger and broader absorption profile with decreasing Mg II FWHM, however the dynamical range in the absorption properties is significantly smaller than the range found for the He II EW or α_{UV1} binning. Similar trends are seen with M_{BH} and L/L_{Edd} . How-

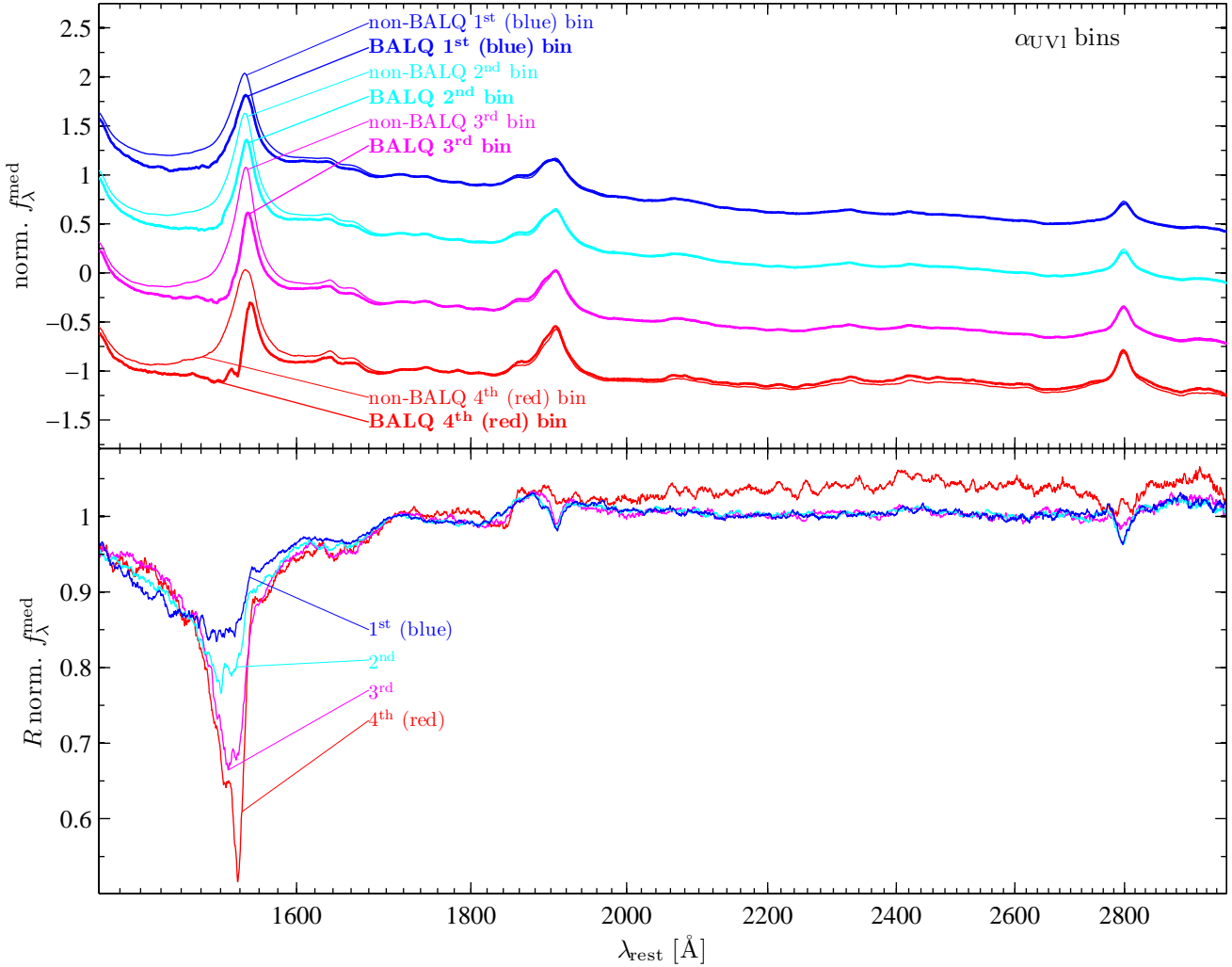


Figure 8. The dependence of the intrinsic absorption on α_{UV1} for the low- z sample. The BALQ and non-BALQ samples are divided into four bins. The 2nd to 4th bin spectra are shifted down for presentation purposes by 0.6, 1.3 and 2, respectively. The C IV absorption profile becomes deeper as α_{UV1} becomes redder at the lower velocities, and remains unaffected at the highest velocities.

ever, these two parameters are strongly correlated with the Mg II FWHM, given the small range in $L(3000\text{\AA})$ (Table 6), and since $L(3000\text{\AA})$ displays no trend, the C IV BAL trend with M_{BH} and L/L_{Edd} is equivalent to the trend with Mg II FWHM. Also, f_{BALQ} is either nearly constant, or shows a range of generally less than a factor of two, which is another indication these four parameters are not the fundamental parameters that underlie the C IV BAL profile. Thus, the He II EW and α_{UV1} appear to be the primary parameters. The possible underlying physical explanation is discussed below (Section 5).

A cautionary note is that one should keep in mind that the evaluated trends with M_{BH} and L/L_{Edd} may not appear significant, since the sample does not cover a large enough dynamical range in L ($\gtrsim 1.5$ dex) to surpass the $\sim \pm 0.5$ dex uncertainty in the M_{BH} prescription calibration (Laor 1998; Krolik 2001; Bentz et al. 2009; Woo et al. 2010).

4.5 Comparison with previous studies

The results of this study are consistent with previous findings. Richards et al. (2002) and Reichard et al. (2003) report that BALQs have slightly weaker He II emission than non-BALQs. Richards et al. (2002) find that their LoBALQ composite has a weaker He II emission than the HiBALQ and non-BALQ composites. This is consistent with most of the LoBALQs residing in our lowest He II EW bin. Reichard et al. (2003) also find the HiBALQs to be redder than non-BALQs, and the LoBALQs to be the reddest. Richards et al. (2003) report a trend between the quasar colour and f_{BALQs} by similarly dividing their sample into four bins. Their f_{BALQs} goes up from ~ 3 per cent for the bluest bin (compared to our 6.9 ± 0.4 per cent) to ~ 18 per cent for the reddest bin (21 ± 1 per cent). A relationship between reddening and the He II EW that breaks for the reddest bin (Table 4) was also previously reported by Richards et al. (2003). The large fraction of LoBALQs found here in bins that have the largest C IV absorption is consistent with Allen et al. (2011), who find that LoBALQs reside

Table 5. The median properties of α_{UV1} and the He II EW binned low- z objects.^a

Class/ α_{UV1}	N_{bin}	N_{obj}	He II EW [Å]	\log $L(3000\text{Å})$ [erg s ⁻¹]	Mg II FWHM [km s ⁻¹]	\log M_{BH} [M_{\odot}]	\log L/L_{Edd}	N_{LoBALs}^b	C IV BAL ^c EW [Å]	$v_{\text{shift}}^{\text{mean}}$ [km s ⁻¹]	σ [km s ⁻¹]	f_{BALQs}^d [per cent]
BALQs	1	99	6.1	45.84	4500	9.08	-0.63	2	6.2	-6000	4200	4.2 ± 0.4
-0.48	2	100	4.2	45.91	4700	9.17	-0.61	0	12.2	-10200	6000	6.3 ± 0.6
	3	100	2.9	45.98	3900	9.06	-0.42	0	13.9	-13000	6300	9.0 ± 0.9
	4	100	1.2	45.94	3300	8.90	-0.32	1	19.5	-13500	5600	14 ± 2
non-	1	2276	6.5	45.77	3900	8.95	-0.54					
BALQs	2	1488	4.3	45.91	4000	9.03	-0.47					
-0.44	3	1015	2.9	45.93	3600	8.98	-0.37					
	4	598	1.2	45.90	3200	8.84	-0.30					
BALQs	1	99	6.5	45.90	4600	9.14	-0.59	0	6.3	-4200	1800	6.1 ± 0.6
-0.76	2	100	4.7	45.97	4300	9.12	-0.51	0	13.0	-10500	6200	11 ± 1
	3	100	3.3	46.04	4300	9.16	-0.50	1	15.9	-10400	5300	15 ± 2
	4	100	1.3	45.97	3400	8.93	-0.29	2	23.7	-13700	6200	24 ± 3
non-	1	1518	6.9	45.88	3800	8.98	-0.46					
BALQs	2	827	4.7	45.96	4000	9.05	-0.44					
-0.76	3	547	3.4	45.97	3700	8.99	-0.38					
	4	318	1.6	45.97	3400	8.92	-0.27					
BALQs	1	99	7.7	45.91	3700	8.95	-0.43	0	8.5	-4200	2000	8.2 ± 0.9
-1.05	2	100	5.1	45.97	4300	9.18	-0.51	0	11.8	-6200	3400	16 ± 2
	3	100	3.4	46.02	3900	9.08	-0.41	1	14.2	-8800	5400	19 ± 2
	4	99 ^e	1.2	45.97	3400	8.95	-0.31	5	22.1	-10900	5900	29 ± 3
non-	1	1107	8.0	45.83	3700	8.93	-0.44					
BALQs	2	539	5.1	45.95	3900	9.04	-0.42					
-1.02	3	414	3.6	45.95	3800	9.00	-0.41					
	4	243	1.3	45.97	3600	8.95	-0.31					
BALQs	1	99	7.7	45.93	3300	8.86	-0.37	3	6.3	-3100	1400	14 ± 1
-1.51	2	100	4.7	46.05	4000	9.09	-0.46	3	18.3	-6900	4700	22 ± 2
	3	100	2.2	46.02	3700	9.05	-0.37	5	14.6	-5700	3700	25 ± 3
	4	100	-0.6	46.03	3700	8.93	-0.33	33	25.9	-9600	5800	31 ± 4
non-	1	620	8.4	45.78	3500	8.85	-0.44					
BALQs	2	362	4.8	45.91	3900	9.01	-0.45					
-1.45	3	307	2.4	45.95	3500	8.93	-0.37					
	4	224	-0.2	45.91	3400	8.87	-0.31					

^a The slope is measured between 1710 and 3000 Å ($f_{\nu} \propto \nu^{\alpha}$).

^b Number of LoBALQs (identified based on a detection of Mg II BAL; Shen et al. 2011) with α_{UV1} and the He II EW within or nearest to the bin range.

^c Measured between $v_{\text{shift}} = 0$ and $-30,000$ km s⁻¹.

^d Measured using the total quasar population. Errors are based on number statistics.

^e An additional BALQ has He II EW smaller by more than 1 Å than the minimal He II EW of the corresponding non-BALQ bin, and is excluded from the BALQ bin.

Table 6. The property median value of Mg II FWHM, $L(3000\text{Å})$, M_{BH} and L/L_{Edd} binned low- z samples.^a

Class	N_{bin}	Mg II FWHM			$\log L(3000\text{Å})$			$\log M_{\text{BH}}$		$\log L/L_{\text{Edd}}$			
		[km s ⁻¹]	N_{obj}	f_{BALQs}	[erg s ⁻¹]	N_{obj}	f_{BALQs}	[M_{\odot}]	N_{obj}	f_{BALQs}	N_{obj}	f_{BALQs}	
BALQs	1	6200	399	13.5 ± 0.7	46.26	399	15.2 ± 0.8	9.47	399	15.5 ± 0.8	0.07	399	12.1 ± 0.6
	2	4500	399	11.2 ± 0.6	46.04	399	13.9 ± 0.7	9.16	399	12.2 ± 0.6	-0.31	399	10.6 ± 0.6
	3	3400	399	9.8 ± 0.5	45.90	399	11.9 ± 0.6	8.91	399	9.4 ± 0.5	-0.55	399	10.8 ± 0.6
	4	2200	399	11.1 ± 0.6	45.66	399	7.4 ± 0.4	8.49	399	9.7 ± 0.5	-0.90	399	11.5 ± 0.6
non-	1	6200	2567		46.26	2225		9.47	2167		0.03	2889	
BALQs	2	4400	3168		46.04	2469		9.17	2876		-0.31	3350	
	3	3400	3693		45.89	2950		8.92	3861		-0.55	3312	
	4	2200	3187		45.60	4981		8.51	3732		-0.91	3084	

^a The property median value is followed by the number of objects in the bin and the observed fraction of BALQs from the total quasar population (in per cent).

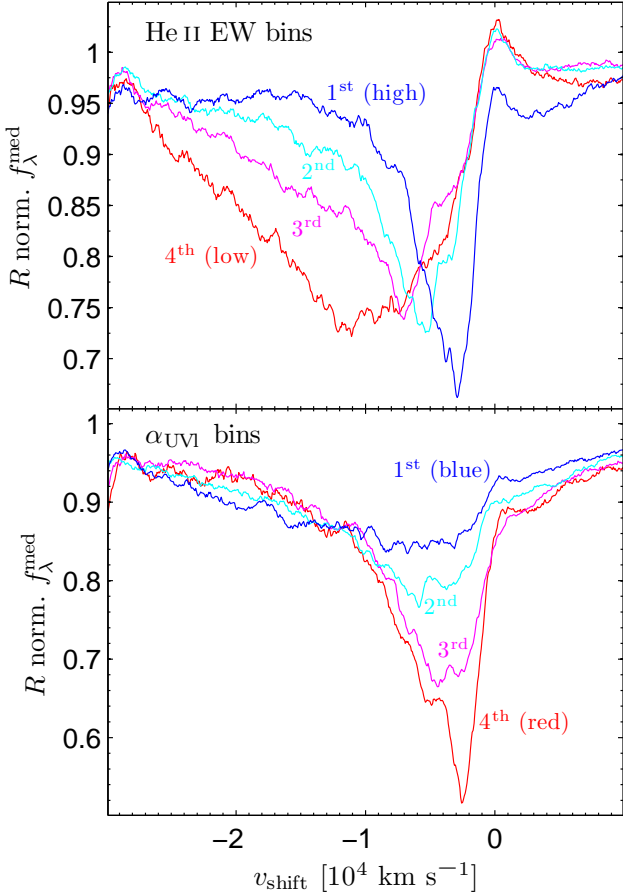


Figure 9. A zoom in on the C IV BAL profile for the composite ratios presented in Figs. 6 and 8. The absorption profile becomes broader and shifts to higher velocities as the He II EW becomes lower, and the absorption becomes deeper at $v_{\text{shift}} > -10,000 \text{ km s}^{-1}$ as α_{UV1} becomes redder.

mainly in objects with a strong and broad C IV absorption (i.e., a high BI; see also Appendix A). Trump et al. (2006) report that BALQs have broader emission lines than non-BALQs, which is consistent with the high Mg II FWHM bin having the largest f_{BALQs} (Table 6). The small range in luminosity of the samples analysed here, prevents detection of the Baldwin effect (e.g., Gibson et al. 2009). In this small range, we find a monotonic growth of f_{BALQs} with $L(3000\text{\AA})$ (from 7.4 ± 0.4 to 15.2 ± 0.8 per cent), which is also reported by Allen et al. (2011) and attributed to a S/N selection effect (see also Knigge et al. 2008). The trend found here is also affected by this effect, since there is a tight correlation in the low- z sample between the spectral S/N and $L(3000\text{\AA})$, with the Spearman rank-order correlation coefficient of $r_S = 0.57$ and 0.66 for the BALQ and non-BALQ samples, respectively (null probability of $\log \text{Pr} < -130$). The median S/N per resolution element after smoothing (Section 2) monotonically increases from $\lesssim 40$ for the lowest- L bin objects to $\gtrsim 100$ for the highest- L bin objects, and some of the absorption is shallow enough to be affected by the S/N level (see Section 4.3).

5 A PHYSICAL INTERPRETATION

We describe below a possible physical context for our findings. First, we suggest how the He II EW, which may be an indicator of the relative strength of the ionizing continuum beyond 4 Ryd, controls the C IV BAL v_{shift} and f_{BALQs} (Section 5.1). Then, we put forward a possible explanation on how α_{UV1} , which may be a reddening indicator, controls the C IV BAL depth and f_{BALQs} (Section 5.2). Finally, we briefly discuss connections to earlier studies (Section 5.3).

5.1 C IV BAL trends with the He II EW

What produces the strong trend between the C IV BAL v_{shift} and the He II EW? The He II $\lambda 1640$ emission line is a recombination line, and provides a measure of the number of He II ionizing photons, i.e. photons above 54 eV, which are absorbed by the BLR gas. The He II EW serves as a measure of the relative strength of the EUV continuum above 54 eV, compared to the near UV continuum. As the BAL outflow increases its radial velocity, its density must drop, and its ionization parameter must rise, potentially leading to complete ionization. Complete ionization halts further acceleration of a radiation pressure driven outflow. A higher He II EW implies a higher ionization parameter at a given outflow density, and thus overionization of the outflow already at a higher density, i.e. at an earlier stage of the wind acceleration, where the outflow velocity is smaller. Even if the outflow is not radiation pressure driven (say it is magnetically driven), a harder ionizing continuum will overionize the outflow already at lower velocities, but due to different qualitative reasons (Fukumura et al. 2010a,b). In the magnetically driven wind model of Fukumura et al. (2010a), the wind density and velocity go as $1/r$ and $1/\sqrt{r}$, respectively, where r is the distance from the ionizing source. The density law implies that the ionization parameter also goes as $1/r$. Thus, in contrast with a radiation driven outflow, here the ionization parameter increases with increasing density and decreasing r i.e., increasing velocity. However, for a harder ionizing continuum, the magnetically driven outflow gets overionized up to a larger r , i.e. down to a lower velocity. Thus, the C IV BAL extends to lower maximal velocities, as expected for a radiation driven outflow, and as found in this study.

To prevent overionization, Murray et al. (1995) suggested the presence of a shielding gas, which blocks highly ionizing photons directed towards the outflow, preventing its overionization. Thus, ions such as C IV remain, despite the rise in the ionization parameter with increasing velocity. The observed relationship between v_{shift} and the He II EW suggests that an outflow overionization does take place when the continuum which illuminates the BLR is hard enough. A large v_{shift} is obtained when the AGN ionizing continuum is soft, possibly enough to prevent overionization. Thus, one may not need to invoke a separate shield to prevent overionization. The suggestion that the observed weakness of the He II EW is sufficient to prevent overionization of the outflow, can be explored quantitatively through photoionization modelling of wind model.

The rise in f_{BALQs} with decreasing He II EW is expected as a larger outflow volume is not overionized, leading to a larger CF of the BAL absorber. A magnetohydrodynamic

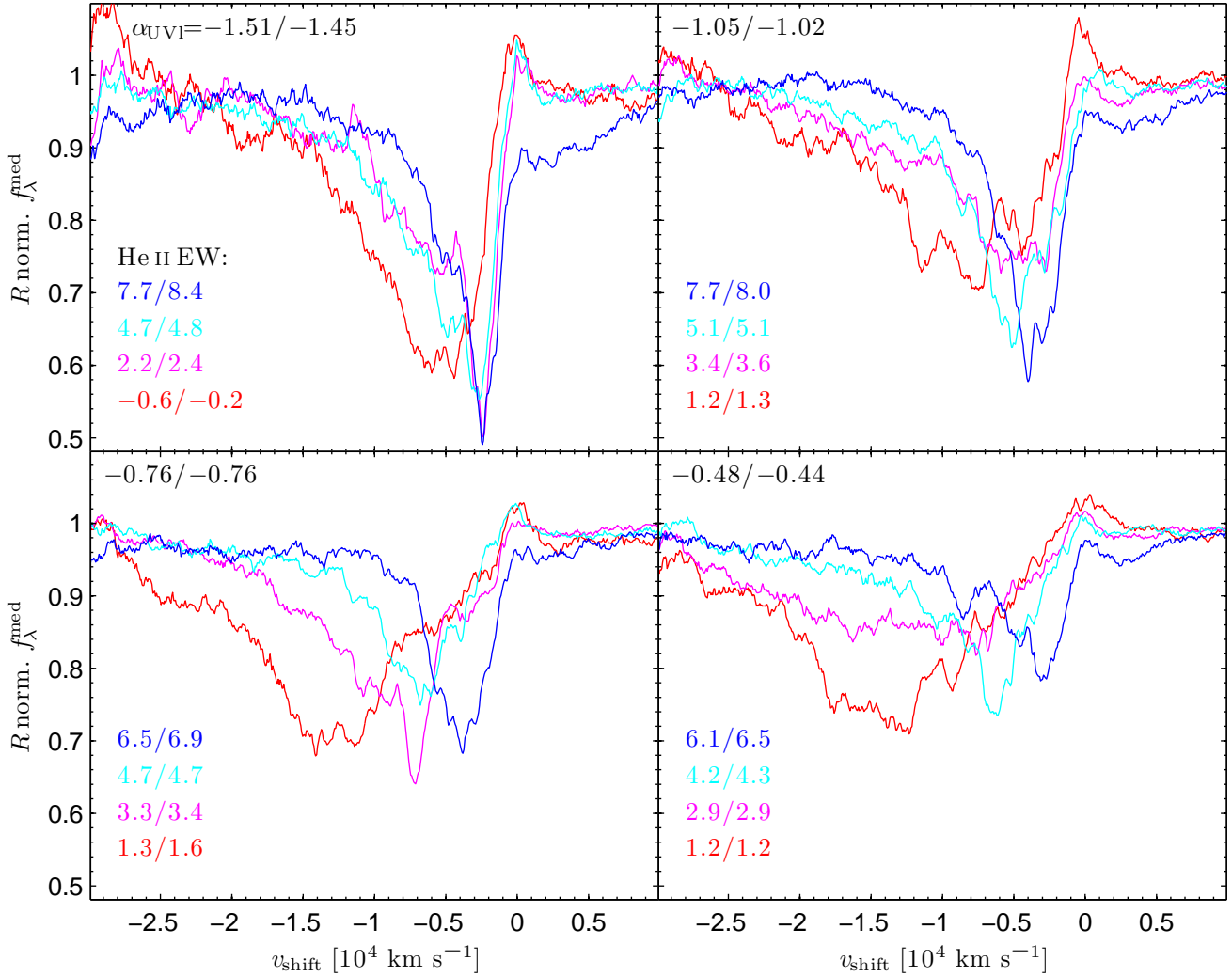


Figure 10. The dependence of the CIV BAL profile on α_{UV1} and the He II EW. The BALQ and non-BALQ samples are first binned into α_{UV1} bins (same as in Fig. 8), and then each α_{UV1} bin is binned based on the He II EW. The upper left corner in each panel provides the median α_{UV1} values for the BALQ/non-BALQ bins used to generate the plotted ratio. The corresponding values for the four He II EW bins (in Å) are indicated in the lower left corner of each panel. Note that all panels have the same y-scale. The CIV BAL profiles become shallower as α_{UV1} becomes bluer, and at each α_{UV1} bin v_{shift} increases as the He II EW decreases. The span in v_{shift} increases as α_{UV1} becomes bluer.

wind model may also produce a similar rise in the CF, as a softer ionizing continuum implies absorbing wind which extends to a smaller r , and may produce a larger CF of the continuum source (Fukumura et al. 2010b). It should be noted that since we are analysing average absorption profiles, the measured CF has an inherent degeneracy between the CF as seen by an observer, the global covering factor of BAL gas (i.e., the CF as seen by the continuum source) and the fraction of BALQs absorbing at a given v_{shift} .

Alternatively, the He II EW may indicate the fraction of the sky of the ionizing continuum covered by the BLR gas Ω instead of a measure of the strength of the EUV continuum above 54 eV. However, there are various relations favouring the interpretation of the He II EW as an ionizing SED indicator. The EUV slope is similar to α_{ox} (Zheng et al. 1997; Laor et al. 1997; Telfer et al. 2002). The α_{ox} is correlated with luminosity (Strateva et al. 2005; Steffen et al. 2006; Just et al. 2007), and luminosity only (Stern & Laor

2012). Similarly, the He II $\lambda 4686$ EW is correlated with luminosity only (Boroson & Green 1992). Thus, the ionizing continuum gets softer with increasing luminosity, leading to the drop in the He II EW with increasing luminosity. Also, lower luminosity objects have a flatter EUV slopes (Scott et al. 2004; cf. Telfer et al. 2002 and Shull et al. 2012). In addition, a BLR Ω trend with luminosity is not expected to directly affect v_{shift} . Future observations can explore directly whether the He II EW is correlated with the EUV slope.

In contrast with the CIV BAL, the NV and OVI BALs do not show a prominent difference in their absorption profiles with the He II EW (Fig. 5). The blue wing of OVI may be affected by N III $\lambda 991$ absorption, and to a lesser extent by C III $\lambda 997$ absorption, while the NV absorption is affected by Ly α absorption. Note also that the NV and OVI ions are produced and destroyed by photons at energies significantly above 54 eV, in contrast with the CIV ion, where these energies (47.9–64.5 eV, Section 3) are just below and above

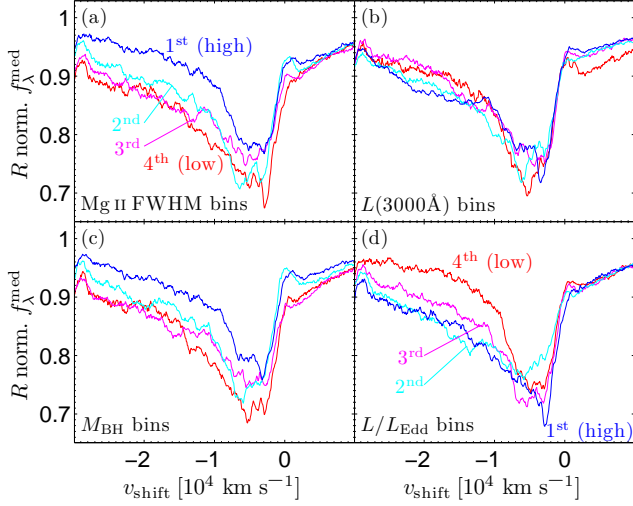


Figure 11. Same as Fig. 9 but the samples are binned based on the Mg II FWHM, $L(3000\text{\AA})$, M_{BH} and L/L_{Edd} . Since the $L(3000\text{\AA})$ range is small (see Table 6), the trend in the C IV absorption with M_{BH} and L/L_{Edd} is a simple outcome of the correlation between the C IV absorption and the Mg II FWHM [panel (a)]. Note that all presented trends are weaker than the trend between the C IV BAL and the He II EW and α_{UV1} (Fig. 9).

4 Ryd. One thus needs to further explore with photoionization calculations the relation between the He II emission EW, and the expected NV and O VI columns relative to the C IV column, as a function of the ionizing spectral shape.

5.2 C IV BAL trends with α_{UV1}

What produces the trend between the absorption depth and α_{UV1} ? The value of α_{UV1} may be interpreted as a viewing angle indicator, if it is affected by reddening, and if the dust tends to reside in the symmetry plane of the system. A support for this scenario is provided by a relation between the optical-UV slope ($\alpha_{\text{o,UV}}$) and the degree of white light polarization, found by Baskin & Laor (2005) in the complete sample of Boroson & Green (1992) PG quasars. A redder $\alpha_{\text{o,UV}}$ is associated with a higher polarization, as expected for a system observed closer to edge on. Baskin & Laor (2005) also show that the change in $\alpha_{\text{o,UV}}$ is consistent with dust reddening (see also Stern & Laor 2012, fig. 17 there). In this interpretation, if there is a clumpy and planar distribution of absorbers, then a redder α_{UV} corresponds to viewing angles closer to edge-on, for which there is a larger probability that our line of sight intersects a UV absorbing gas cloud, and also a dusty gas cloud, i.e. a larger BAL CF and a larger reddening. This explains both the deeper absorption at a given v_{shift} , as a larger fraction of the central source is obscured, and the rise in f_{BALQs} , as a larger fraction of lines of sight passes through an absorber. It is interesting to note that the median absorption depth increases from ~ 5 per cent at the shallowest α_{UV1} , to ~ 20 per cent at the steepest α_{UV1} (Fig. 9), while f_{BALQs} changes similarly from 6.9 ± 0.4 to 21 ± 1 per cent with α_{UV1} (Table 4).

BALQs observed at a larger inclination are also likely to have a larger absorbing column. However, since all lines are most likely saturated, they are not expected to show

a rising absorbing EW. However, X-ray observations may reveal larger absorbing columns in steeper α_{UV1} BALQs.

The inclination interpretation of α_{UV1} implies that BALQs and non-BALQs, at a given α_{UV1} , are observed at the same inclination. What separates BALQs from non-BALQs is then whether an outflow component happens to lie along our line of sight. This scenario requires an azimuthally asymmetric outflow structure, which is also hinted at by the absorption profile variability (e.g., Capellupo et al. 2011, 2012).

The inclination interpretation of α_{UV1} can also explain the lower v_{shift} observed in redder BALQs (Figure 10). Viewing a BALQ close to edge-on increases the probability that the line of sight goes through the base of outflowing absorbing gas, where the projected velocities are lower. A trend indeed observed in recent disc wind simulation by Giustini & Proga (2012, figure 5 there). In contrast, the $v_{\text{shift}} > 10,000 \text{ km s}^{-1}$ part of the outflow shows only a weak α_{UV1} dependence (Figure 9), which suggests the higher velocity outflow component is more spatially extended, and thus less inclination dependent.

We note in passing that binning by the shorter wavelengths α_{UVs} leads to C IV profiles which are very similar to those derived from the He II EW binning, which is in contrast with the result for the α_{UV1} binning. Thus, α_{UVs} is not orthogonal to the He II EW, as α_{UV1} is. This can also be seen in Table 3, where the two α_{UVs} bins show a factor of 4 difference in their median He II EW, in contrast with their similar values in the α_{UV1} bins (Table 4). Thus, α_{UVs} appears to be related to the ionizing SED, as measured by the He II EW, while α_{UV1} is independent of the ionizing SED, and likely provides a measure of the dust extinction (and indirectly the inclination). This qualitative difference is not unexpected, if the optical-UV continuum is produced by accretion disc emission. At long wavelengths, accretions discs are expected to show a universal SED slope, as we are observing the universal slope $L_{\nu} \propto \nu^{1/3}$ part of the disc emission (realistic model slopes are not that flat), which is independent of M_{BH} and L/L_{Edd} . At short enough wavelengths, the slope starts to probe the position of the accretion disc spectral turnover region, and is thus a measure of the ionizing SED (e.g. Davis & Laor 2011).

5.3 The luminosity dependence of v_{max}

Brandt et al. (2000) and Laor & Brandt (2002) found a clear correlation of the maximal outflow velocity v_{max} and the AGN luminosity in soft X-ray weak objects. This relation is quite robust as no Seyfert-level AGN is found to reach $v_{\text{max}} \sim 10,000 \text{ km s}^{-1}$, which is common in BALQs. A pure luminosity trend is simply explained by radiation pressure driven winds (Laor & Brandt 2002, sec. 3.4 there), which gives $v_{\text{max}} \propto L^{1/4}$ for a wind launched from the BLR with a constant force multiplier. The observed steeper relation $v_{\text{max}} \propto L^{0.62 \pm 0.08}$ can be interpreted as an indication of a force multiplier that rises with L (Laor & Brandt 2002). Such a rise may be caused by a softer ionizing SED at a higher L , which produces less overionization, and thus a rise in the force multiplier. A softer ionizing SED at a higher L is consistent with the observed inverse relation between the He II EW and L . The range in AGN luminosity is too small here to test the luminosity dependence of v_{max} (but see ten-

tative evidence in Appendix B). However, the trend found here for v_{shift} with the He II EW, and the strong luminosity dependence of the He II EW, may indicate that the observed relation between v_{max} and the AGN luminosity found by Laor & Brandt (2002), may be partly driven by the v_{shift} versus He II EW relationship found here. A quick inspection of the data in Laor & Brandt (2002) reveals that at a given luminosity, the highest v_{max} is reached by the lowest He II EW objects (which are also the soft X-ray weak quasars). However, a large sample which covers a large range in luminosity and the He II EW is required to clearly separate out the dependence of v_{shift} on L and on the He II EW.

Inspection of Fig. 6 reveals that the C IV emission profiles get weaker and blueshifted with decreasing He II EW, consistent with the finding of Reichard et al. (2003). Richards et al. (2011, fig. 11 there) demonstrate the tight relation between the He II EW and the C IV emission EW and asymmetry, which they interpret as an indication for emission from a wind component in the BLR (see also Leighly & Moore 2004; Kruczek et al. 2011). Above we found that the BAL wind component becomes more prominent as the EUV ionizing continuum gets weaker, which suppresses the overionization of the wind. The suggested BLR wind component may very well be related to the base of the BAL outflow, which is most likely fed by the BLR gas. As the wind accelerates from the BLR, its density and thus emissivity drops, but it remains visible as a BAL through its resonance line absorption. A weaker He II EW implies less overionization, which allows a higher wind emissivity closer to the base of the wind, producing a blueshifted C IV emission component. Unlike the blue wing of the C IV emission that is probably produced by a matter-bounded wind component, the red wing of C IV is probably produced by a non-wind (disc) component (Richards et al. 2011), which is likely radiation bounded. As the relative strength of the EUV ionizing continuum becomes weaker, there is less production of C^{3+} in the radiation-bounded disc component, which leads to a weaker emission in the C IV red wing with decreasing He II EW, as observed.

6 CAN DUST EXTINCTION EXPLAIN THE REDDENING?

The median BALQ SED is redder than the non-BALQ SED (Fig. 1). The difference between the two SEDs appears to be caused by the overall spectral slope, rather than local features. Is the difference in spectral slopes intrinsic to the illuminating source, or is it a result of extinction by foreground dust which is more common in BALQs?

Figure 12 presents corrections of the BALQ composite by several possible dust extinction laws. The BALQ composite is corrected to match the non-BALQ composite by adopting three types of dust extinction laws: Milky Way (MW; Cardelli, Clayton & Mathis 1989), Large Magellanic Cloud (LMC) and Small Magellanic Cloud (SMC; the latter two laws are from Gordon et al. 2003).⁶ The upper panel shows

⁶ All three extinction laws are reported only down to $\lambda_{\text{rest}} = 1000 \text{ \AA}$. Here we assume the analytic functions hold down to $\lambda_{\text{rest}} = 800 \text{ \AA}$. Given the low S/N of the R spectrum at $\lambda_{\text{rest}} < 1000 \text{ \AA}$, the exact form of the extinction law used is not important.

the de-reddening for the high- z sample. One cannot discriminate between the three extinction curves. The lower panel shows the de-reddening for the low- z sample. Here one can clearly exclude a MW- and LMC-like extinction laws by ~ 13 and 9 standard errors in the median R at $\lambda_{\text{rest}} = 2200 \text{ \AA}$, as they produce a strong bump at $2000 < \lambda_{\text{rest}} < 2400 \text{ \AA}$, which is not observed.⁷

A preference for SMC dust was found in various earlier studies of AGN. Sprayberry & Foltz (1992) reach a similar conclusion for the reddening of LoBALQs compared to HiBALQs. Glikman et al. (2012) find that the extinction of dust-reddened quasars in the $\lambda_{\text{rest}} = 4000 \text{ \AA} - 2.4 \mu\text{m}$ range is best described by an SMC-like law (see also a brief overview of additional studies by Pitman, Clayton & Gordon 2000). Hopkins et al. (2004) report that the reddening of quasars in general is consistent with an SMC-like extinction law, while the MW and LMC laws are excluded. Richards et al. (2003) also successfully fit dust-reddened non-BALQs assuming an SMC extinction law. Thus, the result derived here is clearly not new. However, these earlier studies are all based on the observed SED. The observed SED happens to show a shallow and broad dip at $\lambda \sim 2200 \text{ \AA}$, produce by adjacent line emission, which can mimic some effect of the 2200 \AA extinction bump. The ratio plots used here eliminate all the intrinsic spectral features, and thus provide a strong constraint (to a level of ~ 1 per cent) on the possible extinction curve shape associated with the BAL outflow.

The SMC best-fit A_V is evaluated *independently* for the high- and low- z samples. Both samples yield $A_V = 0.06 \pm 0.01$ mag, where the range implies a deviation that is consistent with the standard error in the median R spectrum. The best fit A_V is estimated by eye inspection, requiring the non-BALQ and dereddened BALQ composites to match in wavelength regions unaffected by strong line emission and absorption, i.e. $\lambda_{\text{rest}} \approx 1080$ and 1800 \AA for the high- and low- z samples, respectively. The $A_V = 0.06$ mag reddening fits the top three He II EW bins of the low- z sample (Fig. 6), while the lowest He II EW bin requires $A_V = 0.09$ mag.

The A_V values found here are mostly consistent with what was previously reported for BALQs (Reichard et al. 2003; Maddox et al. 2008; Gibson et al. 2009). Allen et al. (2011) find a trend between A_V and z . The A_V derived here is consistent with the value evaluated by Allen et al. (2011) for $1.6 < z < 2.0$ range (our low- z sample), but it is ~ 3 times smaller than the value for the $3.8 < z < 4.5$ range (our high- z sample). We suspect the $3.8 < z < 4.5$ result of Allen et al. (2011) is an overestimate, as it over-corrects the BALQ N v line emission (see fig. 22 there).

The implied H column is $N(\text{H}) \approx 10^{20} \text{ cm}^{-2}$, using the $N(\text{H}) = 5.8 \times 10^{21} A_V / R_V$ relation (Draine 2011), where $R_V = 2.74$ for the SMC extinction law (Gordon et al. 2003). Given the above constraint on the H^0 column, based on the Lyman edge for a $\text{CF} = 1$ absorber (Section 3.1), the H

⁷ The standard error in the median R is evaluated as follows. First, the standard deviation of f_λ at $1700\text{--}1720 \text{ \AA}$ is calculated for the median BALQ and non-BALQ spectra. Then, the error as a function of λ_{rest} is estimated by assuming the measured error is dominated by photon statistics i.e., the standard deviation is scaled by $\sqrt{f_\lambda(\lambda_{\text{rest}})}$. Finally, the error in the R spectrum is calculated by the standard error progression.

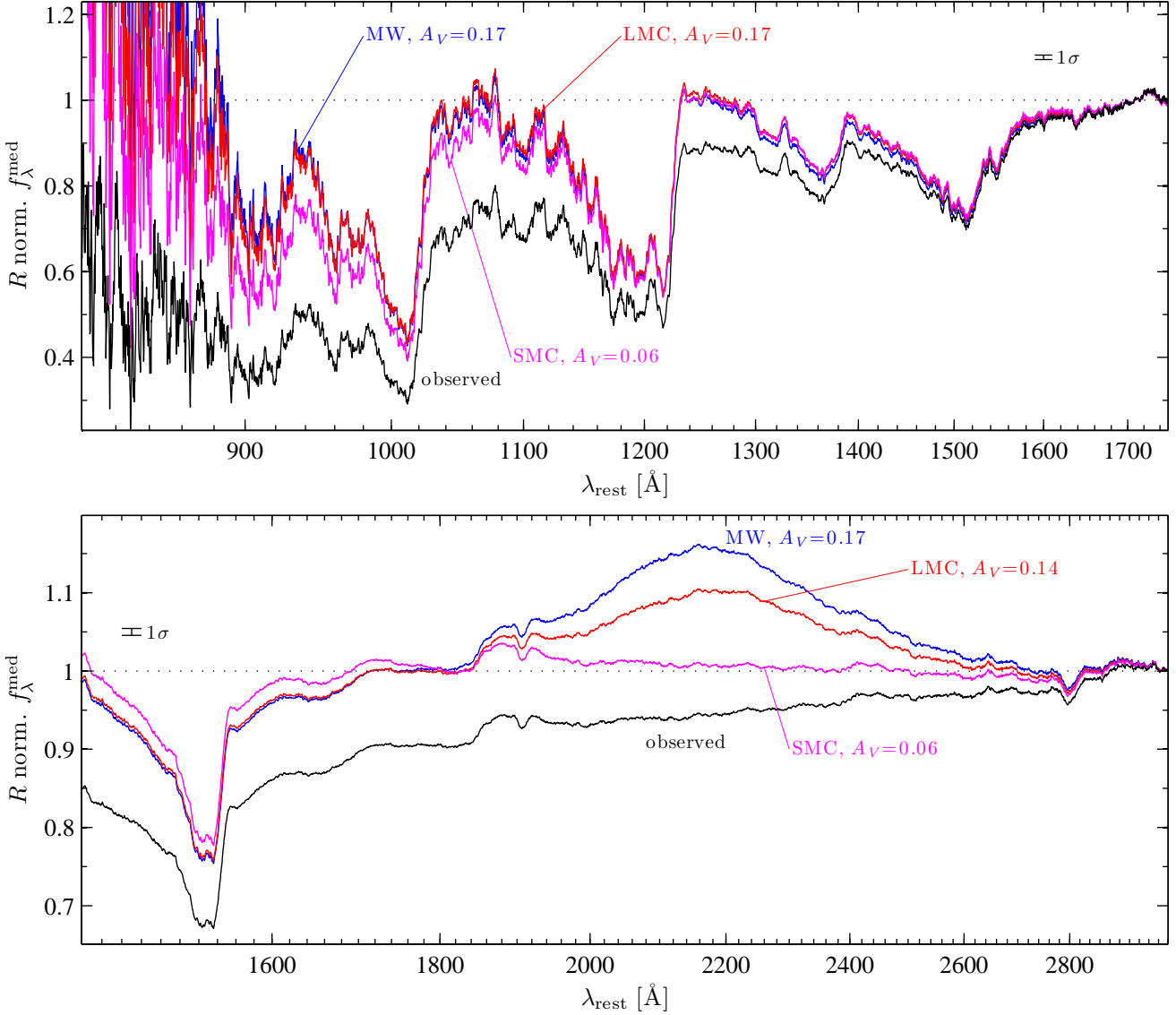


Figure 12. High- and low- z BALQ composites corrected for dust extinction assuming different extinction laws. The low- z composite is normalized at 3000 \AA for presentation purposes. Three extinction-laws are adopted: MW ($R_V = 3.2$) from Cardelli et al. (1989), and LMC ($R_V = 3.4$) and SMC ($R_V = 2.74$) from Gordon et al. (2003). The best fit A_V is estimated by eye inspection (see text). The error bars indicate the standard error in the median value. For the high- z sample (upper panel), all extinction laws are possible, and the MW and LMC extinction corrections are essentially identical. However, the low- z R spectrum (bottom panel) excludes the MW and LMC extinction laws at a high significance level, as they produce a strong bump at $2000 < \lambda_{\text{rest}} < 2400 \text{ \AA}$, which is not observed. Note that both the low- and the high- z composites are consistent with an SMC-like dust extinction with the same A_V value of 0.06 mag.

column associated with the dust must be nearly fully ionized. If the gas is diffuse, the ionization can be maintained by the AGN on the host-galaxy scale. Since non-BALQs are also dust reddened (e.g., Richards et al. 2003; Stern & Laor 2012), the above estimate gives only the excess extinction in BALQs. To get the absolute extinction value, we evaluate the low- z BALQ composite reddening relative to the bluest non-BALQ quartile composite, which is more likely to represent the intrinsic non-reddened SED. This yields $A_V = 0.12$ mag and $N(\text{H}) \approx 3 \times 10^{20} \text{ cm}^{-2}$. A similar analysis for the high- z sample, utilizing the bluest non-BALQ composite, yields $A_V = 0.10$ mag and $N(\text{H}) \approx 2 \times 10^{20} \text{ cm}^{-2}$.

Since the SMC extinction curve is featureless, an intrinsically redder SED for BALQs cannot be excluded. The only

support for the reddening interpretation is the remarkably good match, i.e., a ratio of unity for the dereddened spectra throughout the observed range, from 1000 to 3000 \AA .

7 CONCLUSIONS

We analyse the average absorption properties of high- and low- z samples of BALQs from the SDSS DR7, which cover the wavelength range of $800\text{--}3000 \text{ \AA}$. The absorption properties are derived by taking the ratios of BALQ median spectra to the median spectra of matched samples of non-BALQs. We explore the absorption properties for a number of sub-

samples selected based on various emission properties. We find the following.

(i) No Lyman edge associated with the BAL absorbing gas is detected ($\tau < 0.1$). Thus, on average, $CF \lesssim 0.1$ for a partially ionized absorber in BALQs.

(ii) The average absorption EW increases with the ionization state, from an absorption $EW \lesssim 1 \text{ \AA}$ for C II $\lambda 1335$, to 5.8 for Si IV, 9.3 for C IV, 24.6 for N V and 25.2 \AA for O VI. This may indicate a rise in the covering factor of the BAL outflow with a rise in the ionization state.

(iii) The He II emission EW controls the typical v_{shift} of C IV BAL, which increases from $v_{\text{shift}} < 7000 \text{ km s}^{-1}$ for $EW \gtrsim 6 \text{ \AA}$ to $v_{\text{shift}} > 15000 \text{ km s}^{-1}$ for $EW \lesssim 1 \text{ \AA}$. The He II EW does not affect the absorption depth. The He II EW may indicate the strength of the EUV. A lower He II EW then implies a lower ionization of the outflow, which allows the outflow to reach higher velocities before being overionized. One may not need to invoke a shield to prevent over-ionization of the outflow, as over-ionization may be taking place in high He II EW objects, while in low He II EW objects a shield may not be needed.

(iv) The value of α_{UVI} controls the C IV peak absorption depth, which increases from ~ 0.15 for $\alpha_{\text{UVI}} \approx -0.5$ to ~ 0.45 for $\alpha_{\text{UVI}} \approx -1.5$, at $v_{\text{shift}} < 10,000 \text{ km s}^{-1}$. The value of α_{UVI} does not affect the typical v_{shift} and the absorption profiles at $v_{\text{shift}} > 10,000 \text{ km s}^{-1}$. The value of α_{UVI} may control the average inclination angle of the system, and thus the covering factor and absorbing column for a planar outflow, in particular at the lower velocities, which likely originate close to the base of the outflow.

(v) The He II EW and α_{UVI} also control the fraction of AGN which are BALQs. The fraction rises from 4.2 ± 0.4 per cent in blue ($\alpha_{\text{UVI}} \approx -0.5$) and strong He II ($EW \approx 6 \text{ \AA}$) AGN, to 31 ± 4 per cent in red ($\alpha_{\text{UVI}} \approx -1.5$) and weak He II ($EW \lesssim 1 \text{ \AA}$) AGN. Also, most of the LoBALQs (~ 75 per cent) have He II EW $\lesssim 1 \text{ \AA}$. The He II EW may control the global CF of the BAL outflow, as seen by the ionizing source, as a lower He II EW allows the outflows to extend to larger scales before being overionized. On the other hand, α_{UVI} may control the CF of absorbers along the line of sight, which increases with increasing inclination and the associated reddening.

(vi) The median SED of BALQs is consistent with excess reddening of purely SMC dust with $A_V = 0.06$ mag compared to non-BALQs, or a reddening of $A_V = 0.12$ mag compared to the bluest non-BALQs. Given the lack of associated H I absorption, the dust is embedded in an ionized medium, possibly on the host-galaxy scale. LMC and MW dust are excluded by ~ 9 and 13 standard deviation of the median value, respectively.

The above interpretation of α_{UVI} as a viewing angle indicator can be tested by looking for a trend between α_{UVI} and the continuum polarization, in both BALQs and non-BALQs. One can also look for the expected relationship between α_{UVI} and the X-ray absorbing column in BALQs. The relationships of v_{shift} and f_{BALQs} with the He II EW, together with the inverse relationship of the He II EW with L , imply a steeper than linear rise in the kinetic wind luminosity with L , which may be relevant for feedback in the highest L AGN.

ACKNOWLEDGMENTS

We thank G. T. Richards for many valuable comments. Fruitful discussions with N. Murray and E. Behar are acknowledged. We thank D. Kazanas and the anonymous referee for comments and suggestions. FH acknowledges support from the USA National Science Foundation grant AST-1009628. This research has made use of the Sloan Digital Sky Survey which is managed by the Astrophysical Research Consortium for the Participating Institutions; and of NASA's Astrophysics Data System Bibliographic Services.

APPENDIX A: THE LoBALQ R SPECTRUM

As a sidenote, we use this opportunity to briefly present the LoBALQ median absorption properties based on the low- z BALQ sample. The LoBALQ R spectrum is derived by forming a matched non-BALQ sample, which is matched by the He II EW distribution. Although most of the LoBALQs have small values of He II EW (the whole sample median EW is -1.8 \AA), several LoBALQs (13 out of 56) have somewhat larger He II EW ($> 1 \text{ \AA}$; Table 2), and the matching method used for HiBALQs (i.e., matching in the He II EW range) cannot be utilized here. To produce LoBALQ and non-BALQ composites with a matched He II EW distribution, we carry out the following procedure.

(i) The LoBALQ He II EW distribution is calculated using 2 \AA bins (EW_{bin}). At each EW_{bin} , the number of LoBALQs with He II EW within the EW_{bin} range is divided by the total number of LoBALQs.

(ii) The non-BALQs are assigned to EW_{bin} based on their He II EW value. This yields the measured absolute non-BALQ distribution, $N_{\text{meas}}(EW_{\text{bin}})$.

(iii) The LoBALQ distribution is multiplied by the total number of non-BALQs. This yields the desired absolute non-BALQ distribution, $N_{\text{des}}(EW_{\text{bin}})$.

(iv) The non-BALQs are drawn for each EW_{bin} based on the following three criteria. If $N_{\text{meas}}(EW_{\text{bin}}) = N_{\text{des}}(EW_{\text{bin}})$, then all non-BALQs in that EW_{bin} are drawn. If $N_{\text{meas}}(EW_{\text{bin}}) < N_{\text{des}}(EW_{\text{bin}})$, then all non-BALQs are randomly drawn several times until the number of drawn objects equals $N_{\text{des}}(EW_{\text{bin}})$. If $N_{\text{meas}}(EW_{\text{bin}}) > N_{\text{des}}(EW_{\text{bin}})$, then only $N_{\text{des}}(EW_{\text{bin}})$ of non-BALQs is randomly drawn.

(v) The median spectrum of the drawn non-BALQs is evaluated.

(vi) The resulting median non-BALQ spectrum depends on the particular non-BALQs that are randomly drawn. To eliminate this dependence, the procedure in items (iv) and (v) is repeated 300 times. A median of the 300 median spectra is adopted as the matched non-BALQ composite.

The above procedure produces a matched non-BALQ sample with a median He II EW of -1.3 \AA (compared to -1.8 \AA for LoBALQs). The LoBALQ and the matched non-BALQ composites have α_{UVI} of -1.99 and -1.38 , respectively. The resulting C IV BAL EW, $v_{\text{shift}}^{\text{mean}}$ and σ are 33.9 \AA , $-10,500$ and 5300 km s^{-1} , respectively.

Figure A1 presents the LoBALQ R spectrum corrected for reddening (see below), where we also indicate the laboratory wavelength of Mg II $\lambda\lambda 2796.4, 2803.5$, Al III $\lambda\lambda 1854.7, 1862.8$ and several Fe II absorption lines following Richards

(2001, table 3 there). Note the presence of prominent Fe II BALs in the LoBALQ R spectrum (absorption EW $\gtrsim 7 \text{ \AA}$). The LoBALQ C IV BAL profile is consistent with the relationships, which are found for the low- z HiBALQ sample, between v_{shift} and the He II EW, and between C IV peak absorption and α_{UV1} (Sections 4.1 and 4.2, respectively). The LoBALQ composite has a redder α_{UV1} and a deeper C IV peak absorption than the reddest HiBALQ bin ($\alpha_{\text{UV1}} = -1.99$ versus -1.51 ; compare to Fig. 8). The C IV BAL v_{shift} of LoBALQ composite is similar to v_{shift} of the lowest He II EW HiBALQ bin (Fig. A1), although the LoBALQ median He II EW is lower (0.9 versus -1.8 \AA). The similarity in v_{shift} may be a result of the softer ionizing SED (i.e., lower He II EW for LoBALQs) being ‘too soft’ to produce a C IV absorber at higher v_{shift} . The higher v_{shift} absorber is probably found at larger distances from the ionizing source than a lower v_{shift} absorber, and the soft ionizing SED at those distances results in an ionization parameter that is too low to produce C IV absorption.

A comparison between LoBALQ and HiBALQ composites supports the scenario of a smooth transition between HiBALQs and LoBALQs, where the latter mostly occupy the reddest α_{UV1} and the lowest He II EW parameter-space (Section 4.3). Figure A1 presents the bluest and highest He II EW composite, the lowest He II EW composite (Fig. 6) corrected for reddening (Section 6), and the reddest and lowest He II EW composite. The first composite has EW = 6.1 \AA and $\alpha_{\text{UV1}} = -0.48$ (Table 5), and its R spectrum has no detectable Al III and Mg II BALs. The dip at Mg II laboratory wavelength results from a mismatch in Mg II peak line emission between the matched BALQs and non-BALQs, and likely does not indicate true absorption. The second composite has EW = 0.9 \AA and $\alpha_{\text{UV1}} = -0.96$ (Table 2), and has a marginal Al III BAL and non-detectable Mg II BAL. The third composite has a He II EW = -0.6 \AA and $\alpha_{\text{UV1}} = -1.51$ (Table 5), and its R spectrum has a prominent Al III BAL and a marginal Mg II BAL. There are additional evidence of Al III BAL strength dependence on both He II EW and α_{UV1} . HiBALQ binning based on He II EW (α_{UV1}) produces composites with similar α_{UV1} (He II EW), but with different Al III BAL strength (Figs. 6 and 8). Note that the R spectrum in the Mg II region in Figs. 6 and 8 is dominated by a mismatch in the Mg II peak line-emission, which hinders a detection of any weak Mg II BAL. The Al III BAL appears first, as the ionization parameter becomes lower, since Mg II ions are destroyed by 15 eV photons, while Al III ions are produced by 19 eV photons. As the HiBALQ properties (i.e., He II EW and α_{UV1}) start to resemble those of LoBALQs, low ionization BALs begin to appear in the HiBALQ spectrum, and it becomes more similar to the LoBALQ spectrum. This suggests LoBALQs are the extreme high inclination and soft ionizing SED members of the BALQ population, rather than a distinct population of AGN.

The reddening of the LoBALQ R spectrum is consistent with an SMC dust extinction of $A_V = 0.22$ mag i.e., $E(B-V) = 0.08$. This reddening is similar to $E(B-V) = 0.077$ reported by Reichard et al. (2003) for the SDSS early DR, but is smaller than $E(B-V) = 0.14$ reported by Gibson et al. (2009) for the DR5, where in both studies the reddening is derived by comparing the LoBALQ composite to a composite of the whole non-BALQ sample. If the whole non-BALQ sample, rather than the He II EW matched one,

is utilized to calculate the LoBALQ R spectrum, then the Gibson et al. (2009) result is approximately recovered i.e., $A_V = 0.41$ mag.

APPENDIX B: TENTATIVE EVIDENCE FOR RADIATION PRESSURE DRIVING

Figure B1 presents tentative evidence that the C IV BAL absorber is driven by radiation pressure. The low- z sample is divided into 4×4 bins based on the He II EW and $L(3000\text{\AA})$. The BALQ sample is first divided into four He II EW ‘parent’ bins, and matched non-BALQ bins are constructed (same procedure as in Fig. 6). Then, each He II EW parent bin is divided into four $L(3000\text{\AA})$ bins, with matching non-BALQs from the corresponding He II EW non-BALQ bin. Each BALQ bin contains by construction equal number of objects (~ 100) for all ‘parent’ bins. If the BAL outflow is driven by radiation pressure, then v_{shift} is an increasing function of the force multiplier \mathcal{M} and luminosity L , assuming the outflow launching radius is mainly a function of L (e.g., Laor & Brandt 2002; see also Section 5). \mathcal{M} is mostly set by the SED, and keeping the He II EW constant should also keep \mathcal{M} approximately constant i.e., each panel of Fig. B1 groups objects with a similar \mathcal{M} . The range in $L(3000\text{\AA})$ of our sample is too small ($\lesssim 1$ dex) to produce highly significant differences in v_{shift} between L bins for a given He II EW (i.e., \mathcal{M}). However, note that for the weakest two He II EW bins (Fig. B1, two lower panels), the highest L bin reaches larger v_{shift} than the other three bins. This larger v_{shift} for a larger L is expected, if the BAL outflow is driven by radiation pressure (e.g., Proga, Stone & Drew 1998).

The highest He II EW bin shows very similar v_{shift} as a function of L . Here the peak absorption occurs at $v_{\text{shift}} \sim 3000 \text{ km s}^{-1}$, and the absorbing material may still be confined close to the BLR, i.e. to the base of the outflow. Overionization occurs just as the outflow starts to build up, before radiation pressure has time to build up a significant outflow component, beyond the initial dispersion in the velocity. Only when the He II EW is low enough, to allow significant acceleration, the effect of L starts to appear. Clearly, large samples which span a large range in L (e.g. Laor & Brandt 2002), are needed to explore the radiation pressure interpretation, and clearly separate out the effect of L and the He II EW on the outflow.

REFERENCES

- Allen J. T., Hewett P. C., Maddox N., Richards G. T., Belokurov V., 2011, MNRAS, 410, 860
 Baskin A., Laor A., 2005, MNRAS, 356, 1029
 Baskin A., Laor A., 2012, MNRAS, 426, 1144
 Becker R. H., White R. L., Gregg M. D., Brotherton M. S., Laurent-Muehleisen S. A., Arav N., 2000, ApJ, 538, 72
 Bentz M. C., Peterson B. M., Netzer H., Pogge R. W., Vestergaard M., 2009, ApJ, 697, 160
 Boroson T. A., 2002, ApJ, 565, 78
 Boroson T. A., Green R. F., 1992, ApJS, 80, 109
 Boroson T. A., Meyers K. A., 1992, ApJ, 397, 442
 Brandt W. N., Laor A., Wills B. J., 2000, ApJ, 528, 637

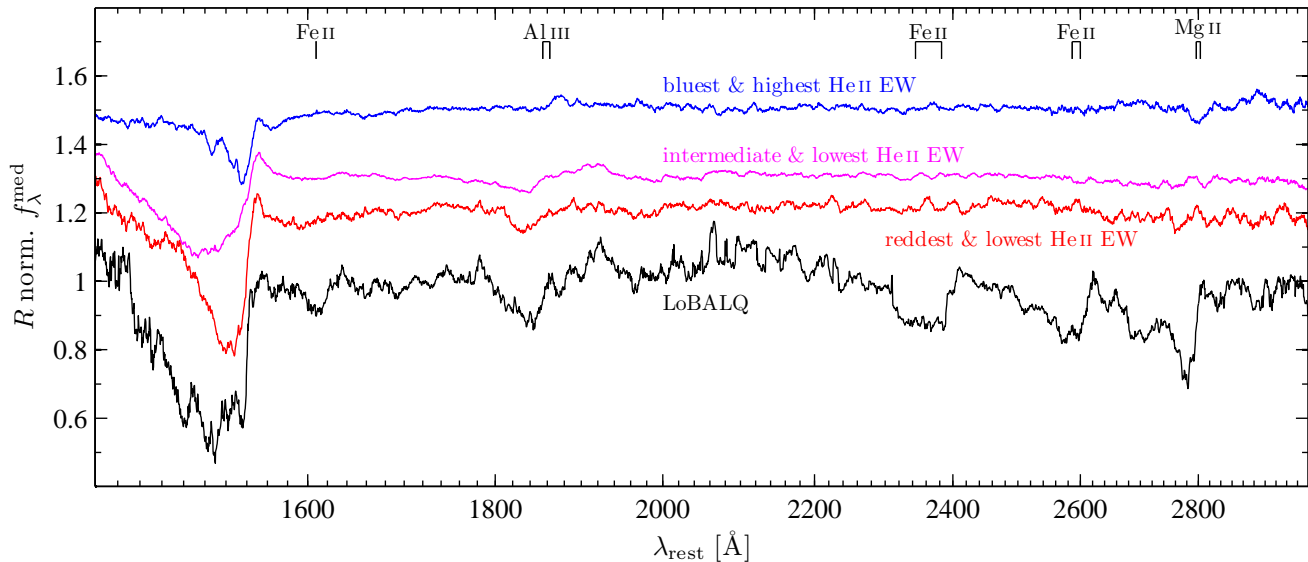


Figure A1. The LoBALQ R spectrum corrected for reddening (black line). The bluest and highest He II EW, the de-reddened lowest He II EW, and the reddest and lowest He II EW composites are presented for comparison (blue, magenta and red line, respectively), and are shifted up for presentation purposes by 0.5, 0.3, and 0.2, respectively. The LoBALQ R spectrum is evaluated by using non-BALQs matched in the He II EW distribution (see text). Note that the de-reddened lowest He II EW bin has an intermediate slope relative to the other two HiBALQ bins. We indicate the laboratory wavelength of Mg II $\lambda\lambda 2796.4, 2803.5$, Al III $\lambda\lambda 1854.7, 1862.8$ and Fe II absorption lines, $\lambda\lambda 1608.5, 2344.2, 2382.8, 2586.7$ and 2600.2 . Note the prominent Fe II BAL troughs that are present in the LoBALQ R spectrum. The LoBALQ sample extends the trend found for the low- z HiBALQs between the C IV absorption depth and α_{UV1} (Fig. 8). The LoBALQ sample has the reddest α_{UV1} and the deepest C IV absorption relative to HiBALQs. A comparison between the different composites indicates that as the HiBALQ properties become more similar to those of LoBALQs (i.e., lower He II EW and redder α_{UV1}), the HiBALQ absorption spectrum starts to resemble the LoBALQ spectrum. The Al III (Mg II) BAL strength increases from a non-detectable to prominent (marginal). The dip at the Mg II laboratory wavelength for the bluest and highest He II EW bin likely does not indicate absorption, since it results form a mismatch in Mg II peak line emission between BALQs and non-BALQs, and has no alignment with the LoBALQ Mg II BAL.

Capellupo D. M., Hamann F., Shields J. C., Rodríguez Hidalgo P., Barlow T. A., 2011, MNRAS, 413, 908
 Capellupo D. M., Hamann F., Shields J. C., Rodríguez Hidalgo P., Barlow T. A., 2012, MNRAS, 422, 3249
 Cardelli J. A., Clayton G. C., Mathis J. S., 1989, ApJ, 345, 245
 Davis S. W., Laor A., 2011, ApJ, 728, 98
 Draine B. T., 2011, Physics of the Interstellar and Inter-galactic Medium. Princeton Univ. Press, Princeton, NJ
 Dunn J. P., Arav N., Aoki K., Wilkins A., Laughlin C., Edmonds D., Bautista M., 2012, ApJ, 750, 143
 Elvis M., 2000, ApJ, 545, 63
 Farrah D., Urrutia T., Lacy M., Lebouteiller V., Spoon, H. W. W., Bernard-Salas J., Connolly N., Afonso J., Connolly B., Houck J., 2010, ApJ, 717, 868
 Farrah D. et al., 2012, ApJ, 745, 178
 Fukumura K., Kazanas D., Contopoulos I., Behar E., 2010a, ApJ, 715, 636
 Fukumura K., Kazanas D., Contopoulos I., Behar E., 2010b, ApJ, 723, L228
 Gibson R. R. et al., 2009, ApJ, 692, 758
 Giustini M., Proga D., 2012, ApJ, 758, 70
 Glikman E. et al., 2012, ApJ, 757, 51
 Gordon K. D., Clayton G. C., Misselt K. A., Landolt A. U., Wolff M. J., 2003, ApJ, 594, 279
 Gordon K. D., Cartledge S., Clayton G. C., 2009, ApJ, 705, 1320
 Hamann F., Korista K. T., Morris, S. L., 1993, ApJ, 415,

541
 Hewett P. C., Foltz C. B., 2003, AJ, 125, 1784
 Hewett P. C., Wild V., 2010, MNRAS, 405, 2302
 Hopkins P. F. et al., 2004, AJ, 128, 1112
 Just D. W., Brandt W. N., Shemmer O., Steffen A. T., Schneider D. P., Chartas G., Garmire G. P., 2007, ApJ, 665, 1004
 Knigge C., Scaringi S., Goad M. R., Cottis C. E., 2008, MNRAS, 386, 1426
 Krolik J. H., 2001, ApJ, 551, 72
 Kruczek N. E., Richards G. T., Gallagher S. C., Deo R. P., Hall P. B., Hewett P. C., Leighly K. M., Krawczyk C. M., Proga D., 2011, AJ, 142, 130
 Laor A., 1998, ApJ, 505, L83
 Laor A., Brandt W. N., 2002, ApJ, 569, 641
 Laor A., Fiore F., Elvis M., Wilkes B. J., McDowell J. C., 1997, ApJ, 477, 93
 Lazarova M. S., Canalizo G., Lacy M., Sajina A., 2012, ApJ, 755, 29
 Leighly K. M., Moore J. R., 2004, ApJ, 611, 107
 Maddox N., Hewett P. C., Warren S. J., Croom S. M., 2008, MNRAS, 386, 1605
 Murray N., Chiang J., Grossman S. A., Voit G. M., 1995, ApJ, 451, 498
 Ogle P. M., Cohen M. H., Miller J. S., Tran H. D., Goodrich R. W., Martel A. R., 1999, ApJS, 125, 1
 Osterbrock D. E., 1989, Astrophysics of gaseous nebulae and active galactic nuclei. Univ. Science Books, Mill Val-

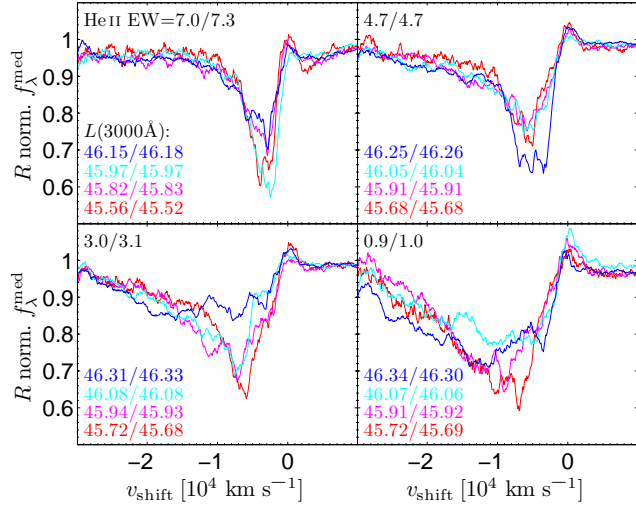


Figure B1. The dependence of the C IV BAL profile on the He II EW and $L(3000\text{\AA})$. The BALQ and non-BALQ samples are first binned into He II EW bins (same as in Fig. 6), and then each He II EW bin is binned based on $L(3000\text{\AA})$. The upper left corner in each panel provides the median He II EW (in \AA) for the BALQ/non-BALQ bins used to generate the plotted ratio. The corresponding values for the four $\log L(3000\text{\AA})$ bins (in erg s^{-1}) are indicated in the lower left corner of each panel. Note that for the lower two He II EW bins (two lower panels), the highest $L(3000\text{\AA})$ composite (blue line) has the deepest absorption trough at $v_{\text{shift}} \lesssim -2 \times 10^4 \text{ km s}^{-1}$.

ley, CA

Peterson, B. M., 1997, *An Introduction to Active Galactic Nuclei*. Cambridge Univ. Press, Cambridge, UK
 Pitman K. M., Clayton G. C., Gordon K. D., 2000, *PASP*, 112, 537
 Proga D., Stone J. M., Drew J. E., 1998, *MNRAS*, 295, 595
 Proga D., Stone J. M., Kallman T. R., 2000, *ApJ*, 543, 686
 Reichard T. A., Richards G. T., Hall P. B., Schneider D. P., Vanden Berk D. E., Fan X., York D. G., Knapp G. R., Brinkmann, J., 2003, *AJ*, 126, 2594
 Richards G. T., 2001, *ApJS*, 133, 53
 Richards G. T., 2012, in Chartas G., Hamann F., Leighly K. M., eds, *ASP Conf. Ser. Vol. 460, AGN Winds in Charleston*. Astron. Soc. Pac., San Francisco, p. 67
 Richards G. T., Vanden Berk D. E., Reichard T. A., Hall P. B., Schneider D. P., SubbaRao M., Thakar A. R., York D. G., 2002, *AJ*, 124, 1
 Richards G. T. et al., 2003, *AJ*, 126, 1131
 Richards G. T., Kruczek N. E., Gallagher S. C., Hall P. B., Hewett P. C., Leighly K. M., Deo R. P.; Kratzer R. M., Shen Y., 2011, *AJ*, 141, 167
 Schneider D. P. et al., 2010, *AJ*, 139, 2360
 Scott J. E., Kriss G. A., Brotherton M., Green R. F., Hutchings J., Shull J. M., Zheng W., 2004, *ApJ*, 615, 135
 Shen Y., Greene J. E., Strauss M. A., Richards G. T., Schneider D. P., 2008, *ApJ*, 680, 169
 Shen Y. et al., 2011, *ApJS*, 194, 45
 Shull J. M., Stevans M., Danforth C. W., 2012, *ApJ*, 752, 162
 Sprayberry D., Foltz C. B., 1992, *ApJ*, 390, 39
 Steffen A. T., Strateva I., Brandt W. N., Alexander D. M., Koekemoer A. M., Lehmer B. D., Schneider D. P., Vignali

C., 2006, *AJ*, 131, 2826
 Stern J., Laor A., 2012, *MNRAS*, 423, 600
 Stocke J. T., Morris S. L., W R. J., Foltz C. B., 1992, *ApJ*, 396, 487
 Strateva I. V., Brandt W. N., Schneider D. P., Vanden Berk D. G., Vignali C., 2005, *AJ*, 130, 387
 Telfer R. C., Zheng W., Kriss G. A., Davidsen A. F., 2002, *ApJ*, 565, 773
 Trump J. R. et al., 2006, *ApJS*, 165, 1
 Urrutia T., Becker R. H., White R. L., Glikman E., Lacy M., Hodge J., Gregg M. D., 2009, *ApJ*, 698, 1095
 Vestergaard M., Osmer P. S., 2009, *ApJ*, 699, 800
 Voit G. M., Weymann R. J., Korista K. T., 1993, *ApJ*, 413, 95
 Weymann R. J., Carswell R. F., Smith M. G., 1981, *ARA&A*, 19, 41
 Weymann R. J., Morris S. L., Foltz C. B., Hewett P. C., 1991, *ApJ*, 373, 23
 Woo J.-H., Treu T., Barth A. J., Wright S. A., Walsh J. L., Bentz M. C., Martini P., Bennert V. N., Canalizo G., Filippenko A. V., Gates E., Greene J., Li W., Malkan M. A., Stern D., Minezaki T., 2010, *ApJ*, 716, 269
 York D. G. et al. 2000, *AJ*, 120, 1579
 Zheng W., Kriss G. A., Telfer R. C., Grimes J. P., Davidsen A. F., 1997, *ApJ*, 475, 469

This paper has been typeset from a \TeX / \LaTeX file prepared by the author.